Geothermics 129 (2025) 103306



Contents lists available at ScienceDirect

Geothermics

journal homepage: www.elsevier.com/locate/geothermics

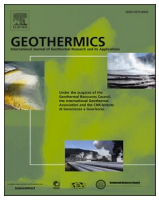

# Petrogenesis and comprehensive thermal assessment of the Dikili-Bergama region, western Anatolia

Tolga Ayzit [a,*], Selçuk Erol [b,c], Alper Baba [a]

[a] Department of International Water Resources, Izmir Institute of Technology, Urla, Izmir 35430, Türkiye
[b] Department of Energy Systems Engineering, Izmir Institute of Technology, Urla, Izmir 35430, Türkiye
[c] Department of Petroleum and Natural Gas Engineering, Middle East Technical University, Ankara, Türkiye

ARTICLE INFO

*Keywords:*
Geothermal exploration
Thermal conductivity
Heat flow analysis
Thermal modeling
Western Anatolia

ABSTRACT

Various methods are available to evaluate the thermal properties and energy potential of geothermal fields. The heat flow method is crucial for thermal modeling and understanding geological evolution. It helps to assess the impact of geological formations on various processes, including hydrocarbon generation and structural modeling. This study focuses on the Dikili-Bergama geothermal region and presents heat flow trends based on thermal modeling. The analysis of volcanic rock petrogenesis data and a thermal model are presented based on data from deep and shallow boreholes. The geothermal gradient is found to vary between 66.28 °C $km^{-1}$ and 121.68 °C $km^{-1}$, according to the interpolated data. Additionally, the study investigates the geochemical and lithological properties of magmatic rocks in the Dikili-Bergama region. The Kozak pluton group's has been measured to have radioactive heat production of up to 7.4 μ$Wm^{-3}$. Thermal conductivity properties and correlations, along with heat flow assessment, contribute to the understanding of geothermal potential. The mean dry thermal conductivity of the rocks in the study area is 2.33 $Wm^{-1}K^{-1}$. The data for the terrestrial heat flow and the radioactive heat flow values are up to 200 m$Wm^{-2}$. The integration of 3D geological models and thermal models has highlighted the south western area of the study as a promising location for unconventional geothermal operations.

## 1. Introduction

Assessing a geothermal field encompasses various methods to evaluate its thermal properties and potential for extracting energy. Geothermal mapping, seismic activity analysis (Suzuki et al., 2020), backward analysis of hydrogeological parameters, volumetric analysis for probabilistic estimates (Athens and Caers, 2019), numerical simulation (Kothari et al., 2024; Kurek, 2021; Lund and Toth, 2021; Pourhakkak et al., 2021), multi-criteria decision making, hydrochemistry, isotopic geochemistry (Wang et al., 2017), geothermometry and multi-well layout simulation is all included in these methodologies (Liu et al., 2022). In addition, techniques such as electromagnetic surveys and geophysical prospection are used to characterize geological heterogeneities and subsurface structures and to map deep reservoirs (Blázquez et al., 2020). These methodologies are of utmost importance in comprehending the thermal structure, composition of fluids, and distribution of temperature within geothermal reservoirs, thereby offering valuable insights for the assessment and management of resources (Blázquez et al., 2020; Huang et al., 2022; Jatmiko et al., 2022; Liu et al., 2022, 2019; Martuganova and Krawczyk, 2021; Pandarinath, 2010; Prol-Ledesma et al., 2016; Putra and Wahyudi, 2021; Qiao et al., 2023; Saibi and Ehara, 2010; Suzuki et al., 2020; Wang et al., 2017; Xing et al., 2015).

The heat flow method is key for thermal modeling and understanding geological evolution (Lucazeau, 2019). It is essential for evaluating the thermal properties of geological formations and their effects on various processes. Heat flow measurements are primary for understanding the geological evolution of planets, including Earth, and for evaluating hydrocarbon generation, structural and thermal modeling, and the distribution of terrestrial heat flow in different geological regions (Fuchs et al., 2023). The method allows for considering the effects of different lithologies on temperature and the influence of geological structures on geothermal fields (Lyu et al., 2020). Furthermore, heat flow measurements are vital for estimating flow in geologic heat pipes, simulating and analyzing thermal deformation, and assessing heat transfer augmentation in various engineering applications (Birkhölzer, 2006;

* Corresponding author.
*E-mail address:* tolgaayzit@iyte.edu.tr (T. Ayzit).

https://doi.org/10.1016/j.geothermics.2025.103306
Received 15 November 2024; Received in revised form 21 February 2025; Accepted 3 March 2025
Available online 7 March 2025
0375-6505/© 2025 Elsevier Ltd. All rights are reserved, including those for text and data mining, AI training, and similar technologies.

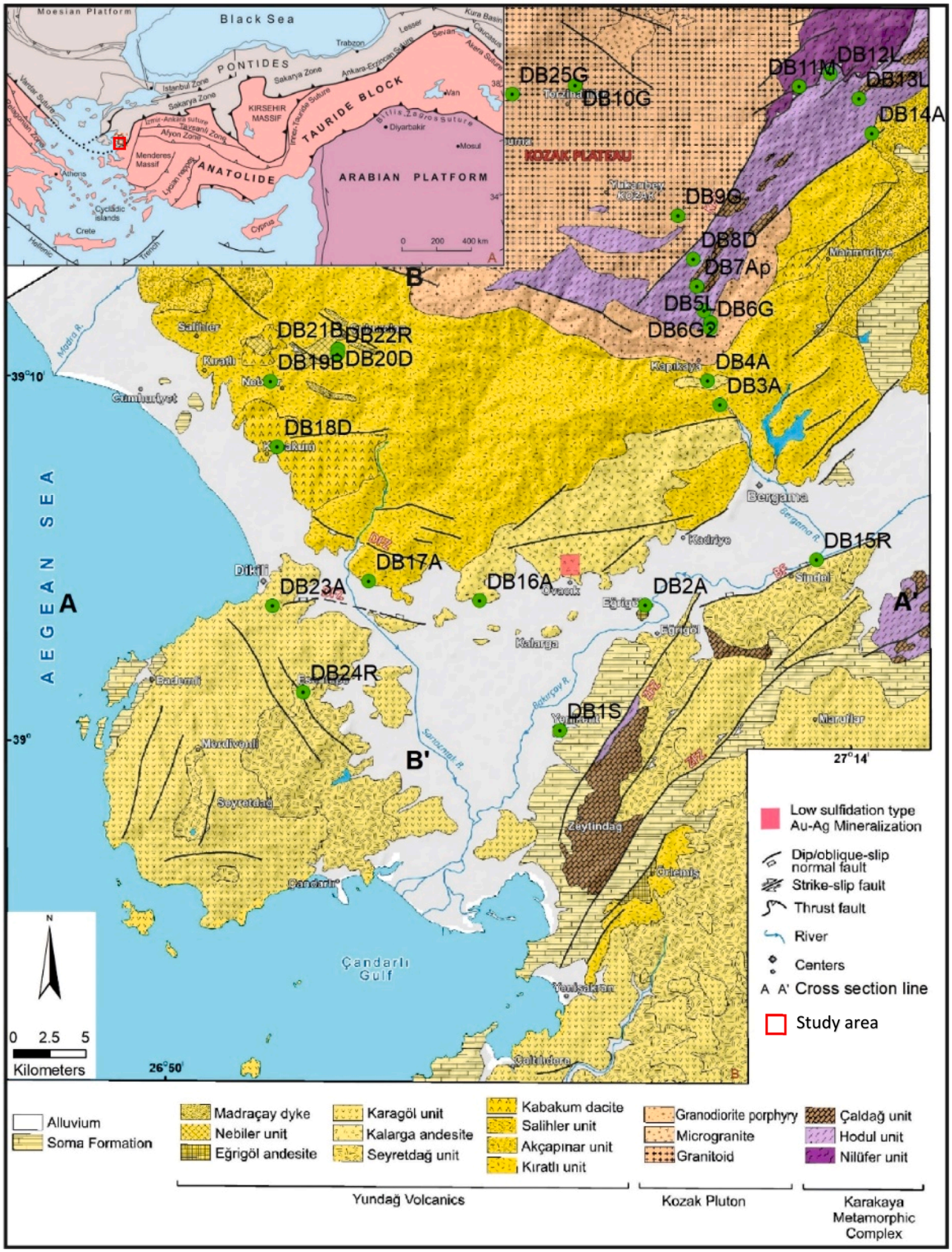


**Fig. 1.** A)Tectonic map of the Türkiye (Okay and Tüysüz, 1999) B) Geology map of the Dikili-Bergama region showing the sampling sites (Akbulut et al., 2023)).

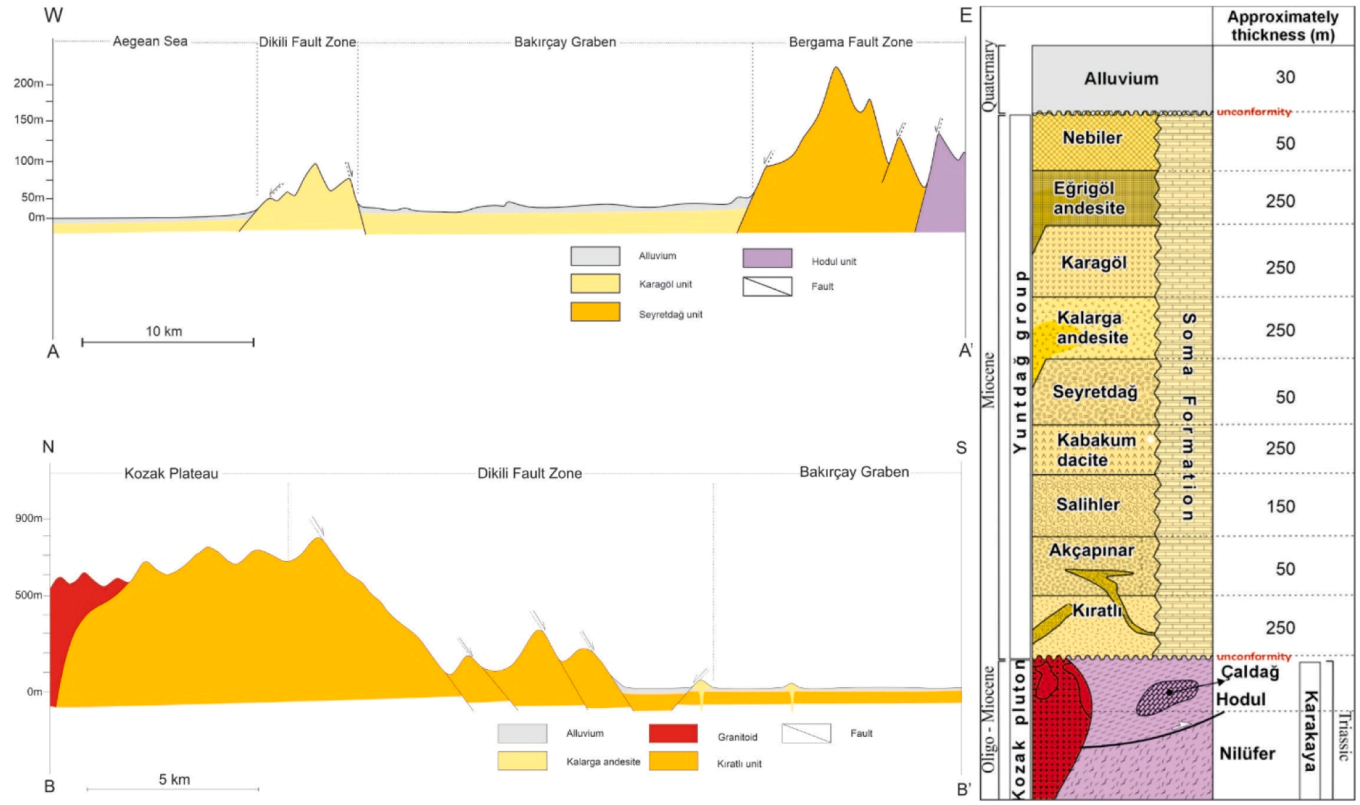


**Fig. 2.** A) Geological cross sectionof west-east direction (A-A') B) Geological cross section of north-south direction (B-B') and stratigraphic column of Dikili-Bergama region.

Chokphoemphun et al., 2015). Heat flow measurements are closely related to the distribution of current terrestrial heat flow and the thermal evolution of basins and uplifts and are used to understand the history of geological formations' tectonic-thermal evolution (Yu et al., 2010). Heat flow data are also used to predict temperature, heat flow, and geothermal gradients (Meixner et al., 2010). This provides reliable information about the thermal structure and evolution of the Earth's crust. The method is also used to estimate fluid flow in thermally disturbed, fractured rocks (Birkholzer, 2005). The comparison and integration of heat flow and radiogenic heat flow data are critical for developing reliable thermal models, offering a comprehensive understanding of the thermal structure, evolution, and heat sources within geological formations (Lucazeau, 2019).

To date, successful unconventional geothermal operations have tended to exploit reservoirs with low porosity and homogeneous crystalline rock (Kong et al., 2021). The average heat flow data for the Cooper Basin and Soultz-sous-Forêts successful unconventional geothermal system fields, which have similar reservoir rocks to the Dikili-Bergama region, are 100 $mWm^{-2}$ (Hogarth and Bour, 2015) and 184 $mWm^{-2}$ (Harlé et al., 2019), respectively. Additionally, the heat flow value may vary depending on the geological environment and location, particularly in regions with tectonic activity. The South China Basin, located in an active tectonic region, has a terrestrial heat flow of approximately 78.3 mWm-2 (Zuo et al., 2020).

The definition of heat flow in western Anatolia has far-reaching implications for various issues, including the study of current extensional tectonic activity in the region and the assessment of its geothermal resources. Studies on the heat flow (Cermak and Hurtig, 1977; Ilkışık, 1992; Tezcan, 1979), geothermal gradient (Korkmaz, 2010; Unalan and Ongur, 1982), and temperature distributions (Erentöz and Ternek, 1968; Karat and Aydın, 2004; Tezel et al., 2013) at different depths have been investigated by many researchers since 1968.

This paper aims to present the trends of heat flow in the Dikili-Bergama geothermal region based on the thermal model and to provide a data set for future detailed geothermal research. First, the petrogenetic data of the volcanic rocks in the region are analyzed. Second, a thermal model is presented using the thermal gradient data obtained from interpolating deep and shallow borehole data in the region. The petrophysical and geochemical properties of rocks sampled from the same points were analyzed to determine their heat flow values for the thermal model.

## 2. Regional background

The Dikili-Bergama region is located in the Sakarya Zone within the western Anatolian Extension Zone. The region is divided into subparallel northeast-southwest trending horsts and grabens formed by major N25–40° E trending oblique faults on the Vardar-İzmir-Ankara Suture Zone (Fig. 1A). The Kozak horst and the surrounding grabens have led to a significant splitting of the E-W trending faults. The geology of the Dikili-Bergama region in western Anatolia is characterized by significant geothermal potential, deep resistive structures, and geological formations indicative of geothermal activity. The geological units in this area comprise four main rock packages separated by stratigraphic, intrusive, and structural contact types in the Dikili-Bergama region. From the oldest to the youngest unit: 1) the Karakaya Complex, 2) the Kozak Pluton, 3) the Yuntdağı Volcanics, 4) the Soma Formation, and the youngest alluvial deposits still forming in the area. On the geological map of the Dikili-Bergama region, 17 different lithologies were identified (Fig. 1B).

The region is located in the transition zone between the Dikili depression and the Bakırçay graben, which is characterized by major fault zones (Özürlan et al., 2006; Turan et al., 2021). The faults in Fig. 2A are generally inclined to the west, while those in Fig. 2B are inclined to the south. The structural elements in the study area are generally inclined towards the southwest, in parallel with the general

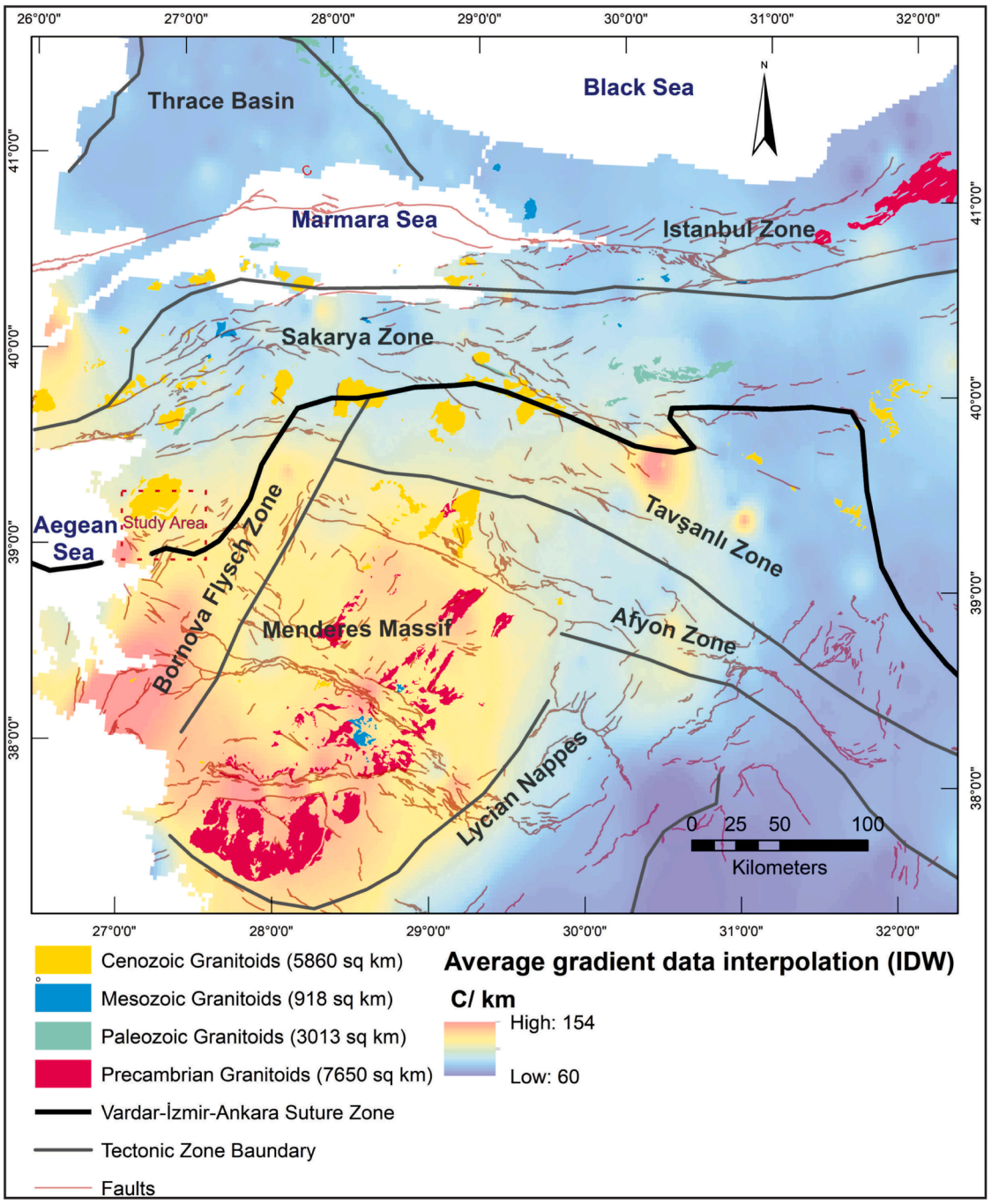


**Fig. 3.** Average of shallow (between 100 - 150 m) and deep (between 1000 - 4500 m) wells gradient data interpolation map (IDW: Inverse Weighted Distance) (modified from Ayzit et al. (2022)).

tectonic regime of western Anatolia. In addition, the region has been associated with counterclockwise micro-block rotations, as indicated by paleomagnetic results that point to the tectonic complexity and geological evolution of the area (Cengiz et al., 2021).

### 2.1. *Karakaya metamorphic complex*

The Karakaya complex in the Bergama-Dikili region consists of three units, namely Nilüfer, Hodul, and Çaldağ. The Nilüfer unit is located on the southeastern edge of the Madra Mountains and covers an area of about 21 km$^2$ in the northeast of the study area (Okay, 2000). It consists mainly of metaophiolitic rocks that have undergone metamorphism in the greenschist facies, together with small amounts of phyllite, marble, and metatuff. The Hodul unit, on the other hand, covers a total of 98 km$^2$ in the NE-SW corridor of the study area. The Hodul unit consists mainly of an olistostromal accretionary complex containing limestone blocks of various sizes in a fine clastic sedimentary matrix. Within the unit, there are generally recrystallized shallow-marine platform-type limestones that can reach dimensions of several tens of kilometers. The Çaldağ unit is accepted as part of this unit. The Çaldağ unit covers a total area of 32 km$^2$ in the study area and is generally present in almost all areas where the Hodul unit occurs. However, the largest outcrops are located in the west of Zeytindağ in the southeast of the area. In this region, the unit is massive and thick-bedded, grey-beige in color and locally filled with spar calcite, partially recrystallized. The geological units forming the Karakaya Complex are generally estimated to be between Permian and

**Table 1**
List of samples classed in sample name, stratigraphic unit, nature of the sampled rock.

| Stratigraphy | | Sample Name | Unit | Nature of the sampled rock |
|---|---|---|---|---|
| **SENOZOIC** | **Miocene** | DB1S | *Soma* | Limestone |
| | | DB2A | *Egrigol* | Andesite |
| | | DB3A | *Kiratli* | Dacite |
| | | DB4A | *Kalarga* | Trachyandesite |
| | | DB14A | *Salihler* | Rhyolite |
| | | DB15R | *Seyretdag* | Rhyolite |
| | | DB16A | *Kalarga* | Dacite |
| | | DB17A | *Kiratli* | Rhyolite |
| | | DB18D | *Kabakum* | Trachyandesite |
| | | DB19B | *Nebiler* | Basalt |
| | | DB20D | *Kiratli* | Tephrite |
| | | DB21B | *Kiratli* | Basaltic trachyandesite |
| | | DB22R | *Kiratli* | Dacite |
| | | DB23A | *Karagol* | Dacite |
| | | DB24R | *Seyretdag* | Rhyolite |
| | **Oligo-Miocene** | DB25G | *Kozak Granitoid* | Granodiorite |
| | | DB26Ank | *Kozak Enclave* | Granodiorite |
| | | DB6G | *Gronodiorite Porphir* | Basaltic trachyandesite |
| | | DB6G2 | *Gronodiorite Porphir* | Andesite |
| | | DB7Ap | *Aplite* | Trachydacite |
| | | DB8D | *Lamprophire* | Basalt |
| | | DB9G | *Arenitized Granite* | Granodiorite |
| | | DB10G | *Microgranite* | Q-rich granitoid |
| **MESOZOIC** | **Triassic** | DB5L | *Hodul* | Limestone |
| | | DB11M | *Niliifer* | Metaophiolite |
| | | DB12L | *Hodul* | Limestone |
| | | DB13L | *Caldag* | Limestone |

Triassic in age. However, it is assumed that the matrix of the complex dates from the Triassic (Akbulut et al., 2023).

### 2.2. Kozak pluton

The granitoid is a product of the partial melting of the accretionary rocks, which is closely linked to the formation of the Vardar-İzmir-Ankara suture zone. The granitoid is a result of regional anatexis and the formation of granitoids. Geochemical similarities include undeveloped Nd isotopic signatures and the strong enrichment of lithophile elements with large ions compared to many high-field strength elements. This observation is consistent with the tectonic structure of the Vardar-İzmir-Ankara suture zone. It indicates that the accretionary rocks are partially fused to form the granitoid. Granitoid is formed from magma sources resulting from the partial melting of various materials, including metasomatized mantle and crustal material. This occurs as part of a post-collisional extension that follows a continent-continent collision (Boztuğ et al., 2008; Graessner et al., 2000).

The Kozak pluton consists mainly of granodiorite with minor amounts of monzonite, quartz monzonite, and diorite. It is metaluminous and mainly high-K calc-alkaline to shoshonitic and I-type. The U-Pb age is calculated to be 24.39 ± 0.18 Ma, and the Ar/Ar age interval of the alteration-free and hand-picked biotite grains from Kozak pluton is 20.00 ± 0.90 Ma - 19.86 ± 0.05 Ma. The TZr value (700–740 °C) indicates that Kozak Pluton was emplaced into magma chambers at shallow to moderate depths (Özdamar et al., 2023).

The Kozak granodiorite is a homogeneous, crystalline volcanic rock mass with high radiogenic heat production, which highlights the geothermal potential of the region. This makes it suitable for enhanced geothermal system (EGS) applications (Hou et al., 2015).

### 2.3. Yuntdağı volcanics

The Yuntdağı Volcanics consist of lavas and pyroclastic rocks that resulted from subduction roll-back and associated back-arc extension. The prevalent lithologies are andesite and dacite lava flows. Rhyolite domes and basaltic andesite-trachyandesite lavas are dominant in the western region of the study area (Aldanmaz, 1998; Altunkaynak and Yilmaz, 1998; Karacik et al., 2007).

This widespread volcanism lasted from the Middle Miocene to the Upper Miocene. Dacitic and rhyolitic lavas and tuffs are its initial expression, although andesitic lavas with tuffs and agglomerates are more common towards the end. Lahars and lava flows are how the volcanic rocks of the area were deposited. Perlite layers and silicified tuffs are also visible in some areas. Based on radiometric age estimations in lavas, 17.6 ± 0.6 Ma was determined to be the age (Borsi et al., 1972; Ercan et al., 1984).

### 2.4. Soma formation

This very widespread formation is a transition to the Yuntdağı volcanics. Its age is in the upper Miocene-Pliocene. This unit consists of an alternation of argillaceous limestone, clay, marl, miltstone, tuffite, sandstone, and conglomerate. It is generally almost horizontally bedded with flexures and fractures in fault zones. In narrow basins, the folds are

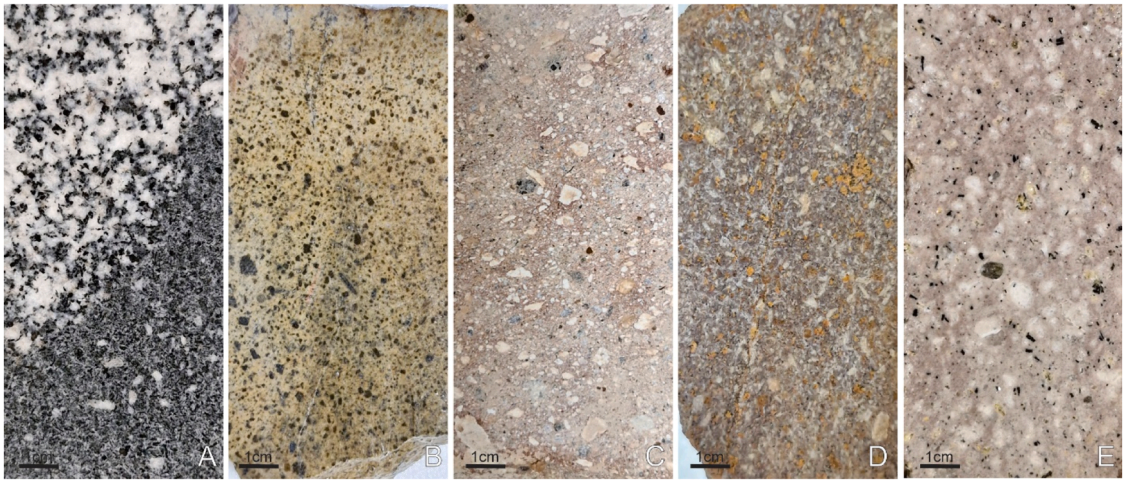


**Fig. 4.** A) Kozak granodiorite and ve enclave B) Basaltic trachyandesite (Max TC in field: 3.02 $Wm^{-1}K^{-1}$) C) Rhyolite (Max porosity in field: 0.41) D) Tephrite (Max RHP in field) E) Dacitic lava consisting of light-colored phenocrysts.

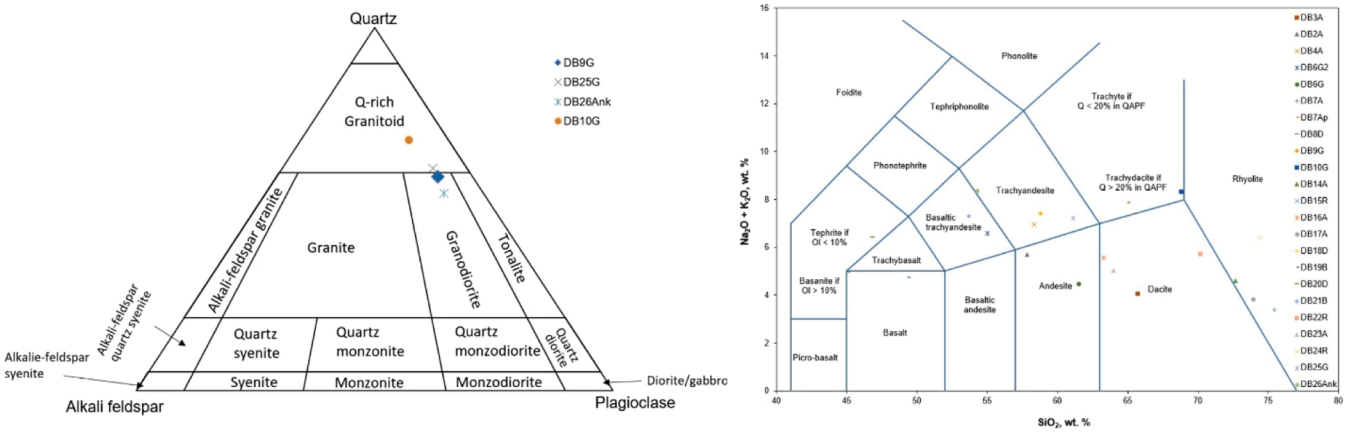


**Fig. 5.** A) Magmatic rock classification diagram (Streckeisen, 1967) (left) B) Chemical classification of volcanic rocks (Bas et al., 1986) (right).

tilted or even overturned by compression. This formation bears coal in the Soma region. The apparent thickness is about 500 m. The Soma Formation was formed in a freshwater lake environment. It is contemporaneous with the Yuntdağı volcanics. Volcanic rocks can also be found in the Soma Formation (Akyürek and Soysal, 1980).

## 3. Tectonic evolution and thermal evaluation

Western Anatolia is characterized by a complex interplay of interrelated geological processes, including extensional tectonic regimes and magmatism. The region was formed by N-S trending extensional tectonic regimes, W-E trending horsts, grabens, and active faults due to the collision of the African, Arabian, and Eurasian plates (Doğru and Pamukçu, 2019; Görür et al., 1995). The tectonic evolution of western Anatolia was strongly controlled by the interplay between regional plate tectonic events and the dynamics of the Earth's mantle, leading to a temporally progressive evolution of Cenozoic magmatism and extension in the region (Dilek and Altunkaynak, 2009). The current tectonic evolution in this region is mainly controlled by the westward movement of Anatolia and N-S extension, both consequences of the same slab roll-back process complicated by several episodes of plate rifting (Roche et al., 2018). In western Anatolia, the difference in gravitational potential energy drives lithospheric kinematics, causing crustal shortening and thickening in response to the relative motion of the Arabian plate. This kinematic behavior is related to the flow of the continental lithosphere towards regions with lower potential energy and contributes to the tectonic evolution of the region (Erman et al., 2022; Mutlu and Karabulut, 2011). The lithospheric structure of western Anatolia is characterized by anisotropic structures, indicating large-scale viscous flow in the lower crust and lithospheric mantle since the Miocene (Roche et al., 2018). In addition, the seismicity and tectonic activity of the region are influenced by the relative NW-directed motion of the Arabian plate, counterclockwise rotation patterns, and the presence of strike-slip faults (Akar et al., 2021; Eken, 2019; Gürer et al., 2018).

Magmatism in western Anatolia is related to the reaction of the Earth's mantle to collisions, plate break-offs, and lithospheric cracks, which lead to the formation of slightly alkaline volcanism. Asthenospheric upwelling caused by the partial detachment of the lithospheric root beneath the orogenic belt has been proposed as the mechanism responsible for the forming of these volcanic rocks (Dilek and Altunkaynak, 2009). The thermal structure of the region is characterized by high thermal values, which has implications for the regional geothermal gradient (Balkan-Pazvantoğlu et al., 2021; Roche et al., 2018).

Fig. 3 demonstrates the conductive heat flow in western Anatolia is high, with mean surface heat flow values of $107 \pm 45$ mWm$^{-2}$, indicating the presence of extensive tectonism and thin continental crust (Erkan, 2015; Komut et al., 2012).

Curie point depth studies conducted in western Anatolia provide different estimates. Estimates of the Curie point depth for western Anatolia range from 8.2 to 19.9 (Aydın et al., 2005; Dolmaz et al., 2005), while another study has found that the Curie point depth for western Anatolia is between 6.21 and 12.41 km. (Bilim et al., 2016).

In Dikili and Bergama there are a total of 27 wells and four natural springs with recorded temperature and flow values. Out of the 27 wells in Dikili, 10 have temperatures exceeding 100 °C, while the wells in Bergama have temperatures ranging from 37 to 62 °C. The highest temperature ever recorded was 131.5 °C. The combined flow rate of the wells in both fields is over 1000 l/s. Among these resources, Kaynarca stands out with a total flow rate of 180 l/s and a temperature of 80 °C. It is considered an extremely high-capacity resource (Baba et al., 2022). While the EC values of the geothermal fluids in Dikili are 410–56,200 μS/cm, EC values of 350–2320 μS/cm were measured in Bergama. The lower EI values of the geothermal fluids of Bergama compared to other areas in the study area can be explained by the proximity of the Dikili region to the sea and the intrusion of saline seawater into the geothermal systems. The waters are of the Na-Cl-$HCO_3$ type, while in other examples they are generally of the Na-$SO_4$–$HCO_3$ type; in other words, it corresponds to the mixed water area, which can be explained by the mixing of the geothermal fluids in the reservoir with fresh groundwater as it rises to the surface. According to the Na-K-Mg triangular geothermometer evaluations, the geothermal fluids correspond to mature waters and partially mature waters. In addition, the temperature isotherm of the geothermal fluids of Dikili-Bergama is between 80 and 200 °C (Baba et al., 2022).

## 4. Materials and methods

### 4.1. Selecting representative rock samples

A total of 27 rock samples were collected from 25 distinct locations to ensure a representative sample of the various lithologies present in the study area (see Table 1). These samples included a range of volcanic and metamorphic rocks encountered along the route to the valley floor, as well as specimens from the Kozak granitoid located in the northern portion of the region. It is important to note that no debris samples were gathered. For this study, volcanic rock nomenclature was based on the comprehensive research conducted by Aldanmaz in 1998. The results were analyzed to ascertain the origins of various parameters associated with regional plate tectonics.

### 4.2. Sample preparation and analysis

Analyzes were performed on eight samples from the Kozak pluton, 14 samples from the Yuntdag volcanics, four samples from the Karakaya

**Table 2**
Definition of volcanic rocks in the Dikili -Bergama region.

| Sample Name | Unit | Thickness (m) | Definition |
|---|---|---|---|
| DB2A | Egrigol Andesite | 250 | Aphanitic andesite with a grayish black color and a fine-grained partially glassy matrix |
| DB3A | Kiratli Dacite | 250 | Porphyritic dacite, whose phenocrysts are composed of plagioclase, amphibole, biotite and to a lesser extent augite and quartz |
| DB4A | Kalarga Trachyandesite | 250 | The predominant mineral in the phenocrysts is plagioclase, besides these, the euhedral/subhedral amphibole and lesser amounts of biotite, augite and a small amount of sanidine-containing rock porphyritic andesite |
| DB14A | Salihler Rhyolite | 150 | Brecciated blocky lava. Phenocrysts of plagioclase, hornblende, biotite and a small amount of sanidine are observed in the matrix, and it contains apatite, zircon and magnetite as accessories |
| DB15R | Seyretdag Rhyolite | 50 | Pyroclastic lava flows consisting of coarse and well-sorted crystalline strength/semi-strength rhyolitic ash flows |
| DB16A | Kalarga Dacite | 250 | The predominant mineral in phenocrysts is plagioclase. It contains euhedral/subhedral amphibole and to a lesser extent biotite, augite and a small amount of sanidine, while apatite and zircon inclusions observed in biotites are accompanied by accessory magnetite |
| DB17A | Kiratli Rhyolite | 250 | Porphyritic lava which phenocrysts are composed of plagioclase, amphibole, biotite, augite and quartz. |
| DB18D | Kabakum Trachyandesite | 250 | Basal lava in grayish black colored aphanitic and/or microporphyritic texture |
| DB19B | Nebiler Basaltic Lava | 50 | Grayish black basalt. In these rocks containing predominantly clinopyroxene (diopsite and augite), microcrystalline plagioclase and forsteritic olivine, minor phases are Fe-Ti oxides (magnetite and ilmenite), phlogopite and biotite rich in Ti |
| DB20D | Kiratli Tephrite | 50 | Lava consisting of brown-colored phenocrysts |
| DB21B | Kiratli Basaltic Lava | 50 | Porphyritic lava which phenocrysts are composed of plagioclase, amphibole, biotite |
| DB22R | Kiratli Dacitic Lava | 50 | Dacitic lava containing plagioclase, hornblende, quartz and biotite |
| DB23A | Karagol Dacite | 250 | Porphyritic textured lava containing plagioclase, hornblende, sanidine, biotite and augite phenocrysts |
| DB24R | Seyretdag Rhyolite | 50 | Pyroclastic lava flows consisting of coarse and well-sorted crystalline strength/semi-strength rhyolitic ash flows |

metamorphic complex and a sample from the Soma formation. All analyzes were carried out elements at the IzTech Integrated Research Centers laboratory.

To obtain reliable thermal conductivity measurements, two planar and parallel surfaces ($12 \times 6 \times 2\ cm$) were cut from each rock sample. The samples were left to dry completely for a week in the sun to enable more reliable thermal conductivity measurements. The thermal transmission coefficient for each sample was calculated by taking the average of at least three measurements from different sides. The KEM QTM 500 device was used to measure the thermal conductivity (Kyoto, 2020). Measurements were conducted at ambient pressure and at the temperature that maximized machine efficiency. Device calibration was verified after each measurement.

The laboratory received each sample in a 2 g tube for analysis using X-Ray Fluorescence Spectrometer (XRF), Inductively Coupled Plasma – Mass Spectrometer (ICP-MS), and Brunauer, Emmet and Teller (BET) techniques after grinding (Pourhakkak et al., 2021). These analyses were provided to detect the chemical compositions, most of the periodic table of elements at nanogram levels per liter, and pore volume of samples, respectively.

Rock classification was performed using XRF results from samples collected from different lithologies. According to the rock classification results, density values were obtained from previous studies (Caineng et al., 2013; Daly et al., 1966; Johnson and Olhoeft, 2017). Porosity was calculated using the pore volume value obtained from BET analysis.

$$Porosity\ (\%) = \left(\frac{Pore\ volume}{Total\ volume}\right) \times 100 \tag{1}$$

The saturated thermal conductivity (λs) was calculated using the geometric mean (Eq. (2)), harmonic mean (Eq. (3)), and Hashin and Shtrikman mean (Eq. (4)) equations by using the determined porosity (ϕ) and measured dry thermal conductivity (λd) values (Fuchs et al., 2018, 2013).

$$\lambda_s = \lambda_d^{1-\phi} \times \lambda_w^{\phi} \tag{2}$$

$$\lambda_s = \frac{1-\phi}{\lambda_d} + \frac{\phi}{\lambda_w} \tag{3}$$

$$\lambda_s = 0.5 \times \left\{ \left( \lambda_d + \frac{\phi}{\frac{1}{\lambda_w - \lambda_d} + \frac{1-\phi}{3\lambda_d}} \right) + \left( \lambda_w + \frac{1-\phi}{\frac{1}{\lambda_d - \lambda_w} + \frac{\phi}{3\lambda_w}} \right) \right\} \tag{4}$$

thermal conductivity of air $\lambda_a = 0.025\ W\ m^{-1}\ K^{-1}$ (Gröber and Erk, 2013) and water $\lambda_w = 0.604\ W\ m^{-1}\ K^{-1}$ (Lemmon, 2010)

Radiogenic heat production ($A$) and radioactive heat flow ($Q$) were calculated according to Rybach (1976) and Lachenbruch (1968), respectively.

$$A\left(\mu W m^{-3}\right) = 10^{-2} \times \rho \times \left(9.52C_u + 2.56C_{Th} + 3.48C_K\right) \tag{5}$$

where ρ ($g/cm^3$) is the density of the rock (average density for granitoid is 2.7 $g/cm^3$), and $C_U$, $C_{Th}$ and $C_K$ are the concentrations (ppm).

$$Q = Q_0 + D \times A \tag{6}$$

where $Q$ is the heat flow at the surface, $Q_0$ is an initial value of heat flow unrelated to the specific decay of radioactive element at a particular time, $D$ is the thickness of rock (~10 km), $A$ is the radioactive heat production. Since the thin crustal thickness (~25 km) observed in the region, the background heat flow value is 40 $mWm^{-2}$.

### 4.3. Modelling

The integration of 3D geological modeling with geothermal field analysis has proven to be an effective method for assessing geothermal reserves and calculating heat flow in geothermal regions. This section discusses the volumetric 'heat in place' method, analytical approaches, and thermal modeling, offering a comprehensive evaluation of geothermal reserves and their associated heat flow (Zhu et al., 2020). In this study, a thermal model was developed using data from both shallow and deep wells in the area. Thermal conductivity, porosity, and values

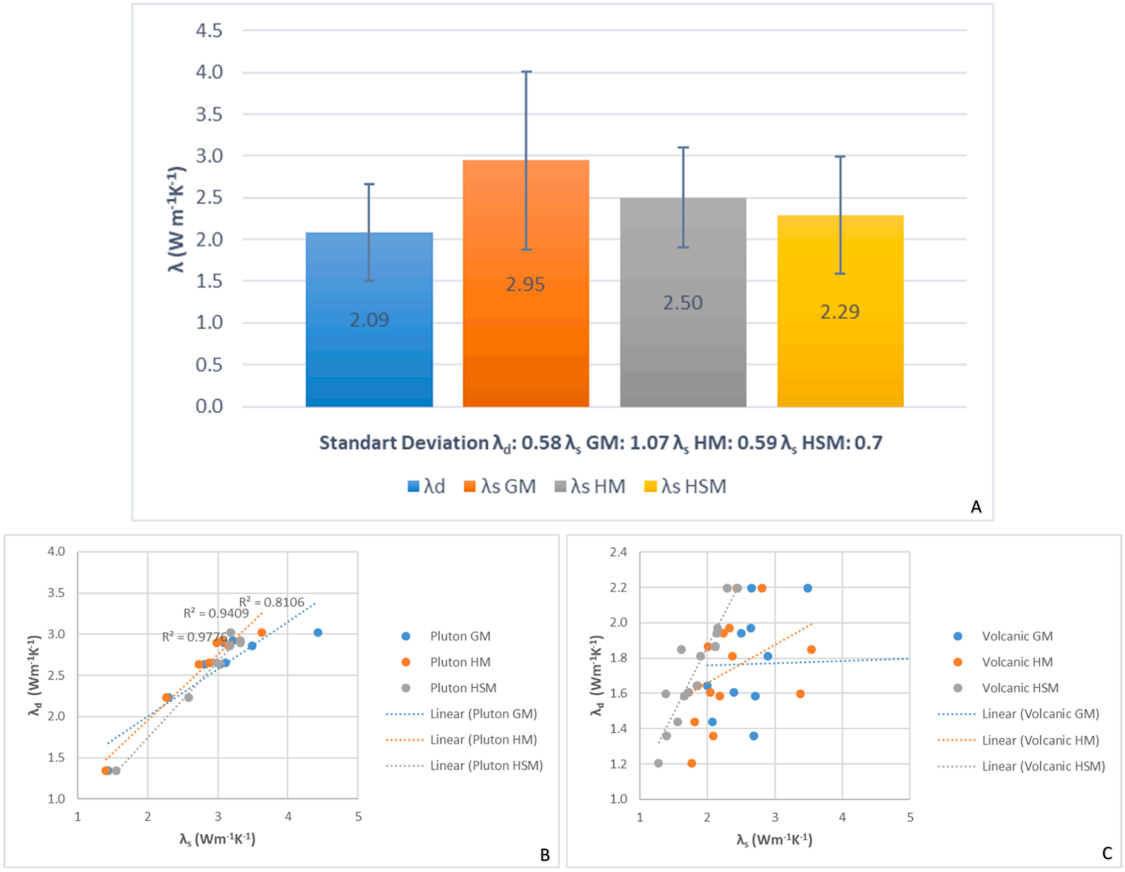


**Fig. 6.** A) Correlation of error bar, mean value and standard deviation values of two-phase system models. $\lambda_d$: Measured thermal conductivity. GM: Geometric mean HM: Harmonic mean HSM: Hashin and Shtrikman mean B) Measured thermal conductivity ($\lambda_d$) and water-saturated thermal conductivity ($\lambda_s$) correlation and $R^2$ values of two-phase system models for plutonic rocks C) Measured thermal conductivity ($\lambda_d$) and water-saturated thermal conductivity ($\lambda_s$) correlation and $R^2$ values of two-phase system models for volcanic rocks.

for radioactive heat flow of each geological unit were calculated, leading to the derivation of depth-dependent heat flow-temperature relationships in the model. Additionally, a detailed thermal model and a general conceptual model of potential geothermal sites in the region are presented. The modeling was conducted using ArcGIS (ArcGIS, 2023) and Leapfrog Energy (Seequent, 2023) software. The methodology involves examining the tectonic evolution and thermal properties of western Anatolia, the geology of the study area, sample locations with lithological characterization, geochemical classification, thermal evaluation, heat flow analysis, and radioactive heat production. This comprehensive approach culminates in the creation of the thermal model and the identification of heat flow trends.

## 5. Results and discussions

### 5.1. Lithological characteristic of magmatic rocks

The Kozak pluton is a type of granodiorite that is light in color. Feldspar, biotite, quartz, and hornblende crystals are visible in the macro samples. The granodiorites exhibit a porphyritic texture towards the edges of the massif and occasionally transform into fine-grained granodiorite porphyries. At the contacts of the pluton with the surrounding rocks, there are skarn zones and magnetite, which are products of contact metamorphism, and occasionally pyrite and chalcopyrite mineralizations. Additionally, there are aplite veins of varying lengths and thicknesses within the Kozak pluton (Fig. 4).

The Kozak pluton was examined, and samples of granodiorite, microgranite, arenitic granite, and enclaves were analyzed. The microgranite is classified as a Q-rich granitoid according to the Streckeisen (1967) classification due to its high $SiO_2$ content. The other samples can be classified as granodiorite (Fig. 5A).

The Yuntdag volcanics cover a large area in the study region and typically exhibit fine-grained, porphyritic, hyaloporphyritic, and microlithic textures. The volcanites are classified as andesite, dacite, trachyandesite, rhyolite, basalt, basaltic trachyandesite, and tephrite according to the Bas et al. (1986) classification (Fig. 5B). The chemical composition of the dacitic lavas is comparable to that of the Kozak pluton. Considering the diagram, we can say that the volcanics are high-K calc-alkaline and partially shoshonitic. These rocks are typically found in regions where magma from the mantle interacts with the continental crust and are associated with subduction zones. They tend to have higher potassium/sodium ratios compared to calc-alkaline rocks. It can be observed that the $K_2O/SiO_2$ ratio remains constant as $SiO_2$ increases in volcanic rocks. This indicates that the volcanic rocks belong to the calc-alkaline group formed within the continents and are composed of lavas originating from the continental crust. The common crystals observed in Yuntdağ volcanic units are quartz, plagioclase, and biotite, and are generally between 50 and 250 m thick (Table 2).

### 5.2. Thermal conductivity properties and correlations

Thermal conductivity measurements have been analyzed across volcanic and plutonic rocks. For volcanic rocks, dry thermal conductivity values range from 1.2 $Wm^{-1}K^{-1}$ to 2.2 $Wm^{-1}K^{-1}$, with the most conductive sample originating from the Nebiler unit, characterized by a basalt composition. In contrast, samples from the Kozak pluton group exhibited dry thermal conductivity values between 2.2 $Wm^{-1}K^{-1}$and 3 $Wm^{-1}K^{-1}$. The average dry thermal conductivity measured for

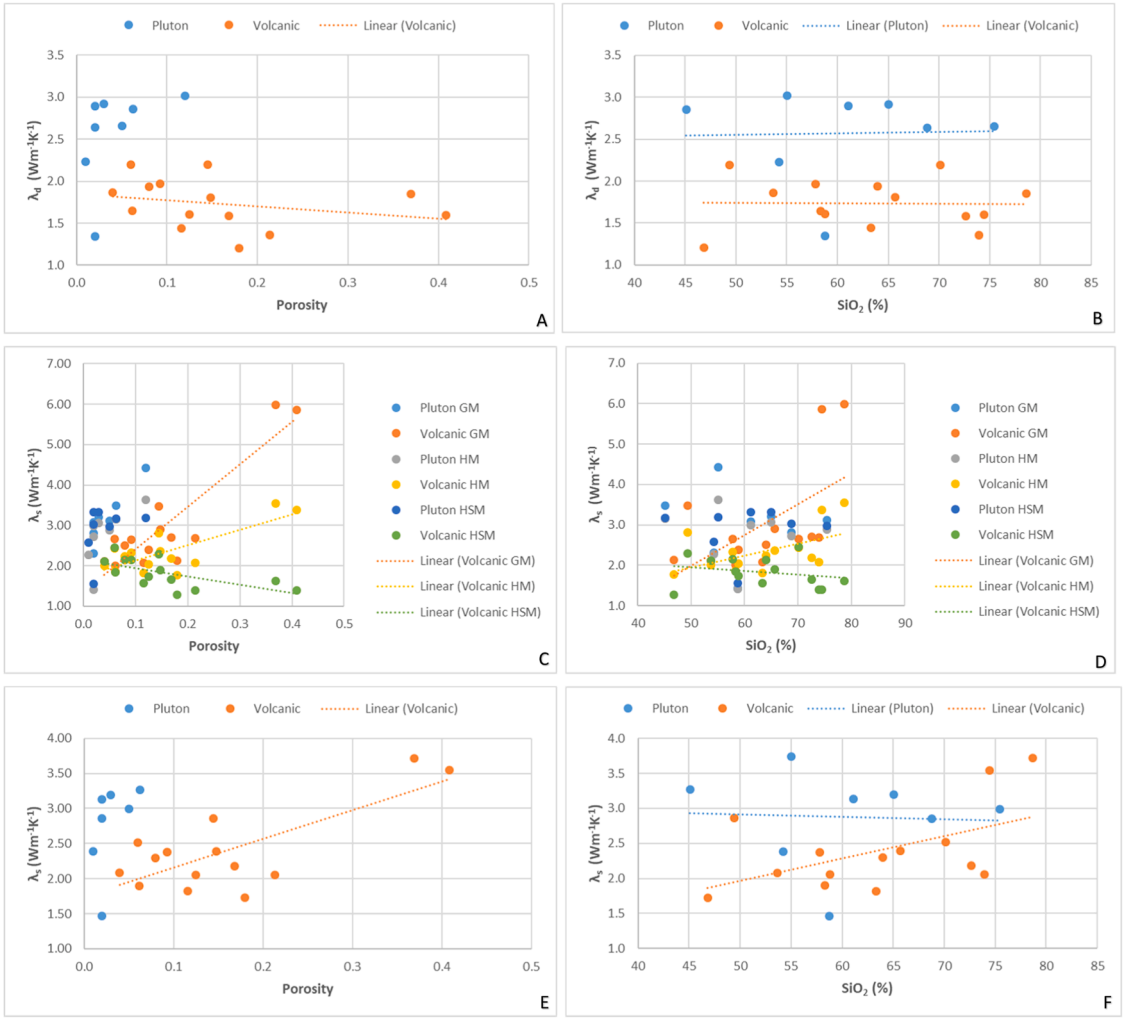


**Fig. 7.** A) Measured thermal conductivity ($\lambda_d$) and porosity correlation for plutonic and volcanic rocks B) Measured thermal conductivity ($\lambda_d$) and $SiO_2$ content correlation for plutonic and volcanic rocks C) Correlation of calculated water saturation thermal conductivity values and porosity of two-phase system models. $\lambda_s$: Water-saturated thermal conductivity GM: Geometric mean HM: Harmonic mean HSM: Hashin and Shtrikman mean D) Correlation of calculated water saturation thermal conductivity values and $SiO_2$ content of two-phase system models. $\lambda_s$: Water-saturated thermal conductivity GM: Geometric mean HM: Harmonic mean HSM: Hashin and Shtrikman mean E) Correlation of calculated water saturation thermal conductivity average values and porosity of two-phase system models. F) Correlation of calculated water saturation thermal conductivity average values and $SiO_2$ content of two-phase system models.

metamorphic rocks stands at 2.7 $Wm^{-1}K^{-1}$, indicating a similarity to the conductivity of plutonic rocks.

Porosity plays a critical role in these measurements: volcanic rocks exhibit an average porosity of 16 %, whereas plutonic and metamorphic rocks average at 4 % and 2 %, respectively. Given an understanding of effective porosity, various models can be employed to estimate the saturated thermal conductivity based on the corresponding dry thermal conductivity (Fuchs et al., 2013).

The saturated thermal conductivity of magmatic rocks was evaluated using robust models, specifically the geometric (GM), harmonic (HM), and Hashin-Shtrikman (HSM) two-phase system models (Chopra et al., 2018; Fuchs et al., 2018; Ray et al., 2015). The results corroborate prior research regarding the efficacy of these models. Average water-saturated thermal conductivity values were determined as 2.29 $Wm^{-1}K^{-1}$ for HSM, 2.50 $Wm^{-1}K^{-1}$ for HM, and 2.95 $Wm^{-1}K^{-1}$ for GM (Fig. 6). Analysis of standard deviation indicates that the HM model is the most reliable for assessing the saturated thermal conductivity of igneous rocks.

Evaluation based on $R^2$ values suggests that both the HSM and HM models outperform the GM model in reliability, with $R^2$ values recorded at 0.97, 0.94, and 0.81, respectively. Individual calculations for water-saturated thermal conductivity of plutonic and volcanic rock samples reveal a less uniform distribution for volcanic rocks due to their elevated porosity. Nevertheless, the HSM model offers a more coherent representation when determining the water-saturated thermal conductivity of volcanic rocks, as illustrated in the accompanying figures.

The dataset reveals a negative correlation between dry thermal conductivity values and porosity in volcanic rocks with high porosity. As porosity increases, the thermal conductivity of dry samples tends to decrease. This is because the thermal conductivity of air in cavities is lower than that of water in saturated samples. Additionally, the shape and structure of particles in rocks influence the relationship between thermal conductivity and porosity in both dry and saturated states (Zhu et al., 2020). Conversely, it has been observed that the thermal conductivity of plutonic rocks with low porosity is independent of porosity (Fig. 7A). The thermal conductivity of water-saturated plutonic rocks does not show a pattern related to porosity. Different trend lines emerge for the thermal conductivity values of water-saturated volcanic rocks when calculated using the GM, HM, and HSM models. While the GM and HM models exhibit direct proportionality to porosity, the HSM model shows a negative correlation (Fig. 7C). When analyzing the average saturated thermal conductivity values of different models (GM, HM,

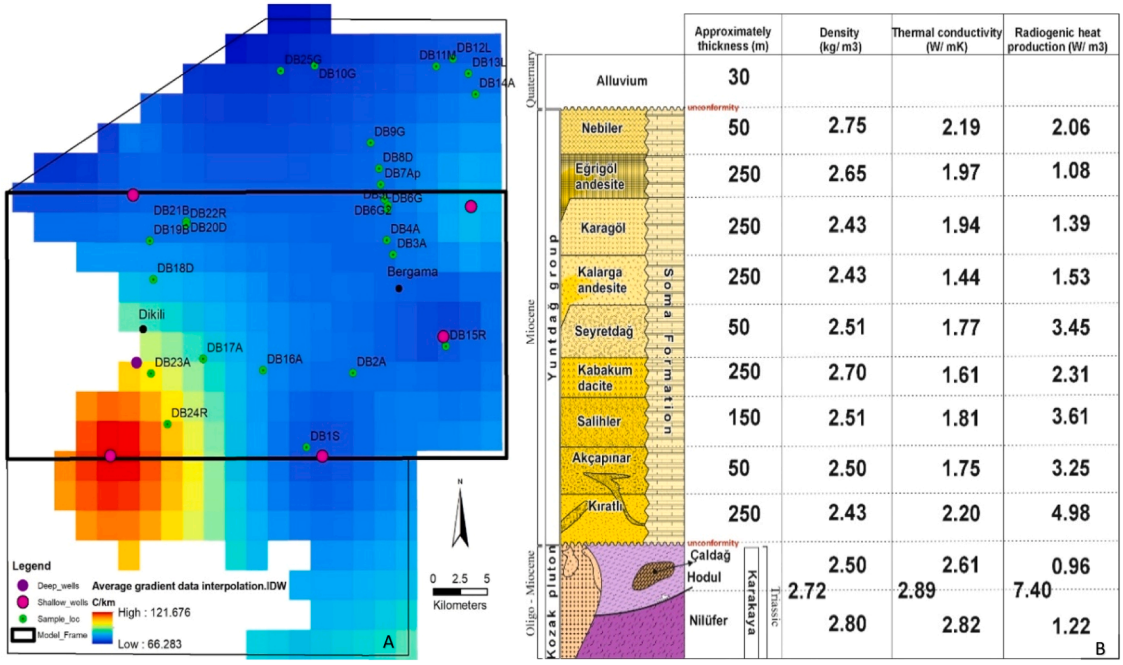


**Fig. 8.** A) Average gradient data interpolation of the study area (left) B) Thickness, density, measured thermal conductivity and RHP value for litologies (right).

HSM), plutonic rocks with relatively low porosity display an irregular distribution, whereas volcanic rocks with higher porosity show a positive correlation (Fig. 7E). Geochemical analyses indicate that $SiO_2$ values in plutonic and volcanic rock samples range between 45 % and 80 %. The $SiO_2$ content in igneous rocks can influence their thermal properties (Stolper et al., 2013). The relationship between measured thermal conductivity and $SiO_2$ was examined, but no significant trend line was identified, despite a generally positive correlation between $SiO_2$ and thermal conductivity (Fig. 7B). However, the HSM model shows a negative correlation with $SiO_2$ content, whereas the GM and HM models exhibit positive correlations. A similar relationship is observed between porosity and water-saturated thermal conductivity (Fig. 7D). Considering the average of the models used, while the thermal conductivity values of water-saturated plutonic rocks display an irregular distribution, a positive correlation is evident between the thermal conductivity of water-saturated volcanic rocks and $SiO_2$ content (Fig. 7F). Volcanic rocks that are rich in $SiO_2$, such as quartz, demonstrate higher thermal conductivity due to the intrinsic thermal properties of silica-rich minerals (Feng et al., 2020). This results in a positive correlation between silica content and thermal conductivity values in a water-saturated state. The presence of various minerals with differing thermal conductivities in plutonic rocks contributes to an uneven distribution of thermal conductivity values when saturated with water. Additionally, the heterogeneity in mineral content and structure within plutonic rocks can further affect the variability of their thermal conductivity distributions.

### 5.3. Thermal assessment through heat flow

The most reliable method of calculating heat flow in a geothermal area is a critical factor in geothermal exploration and resource evaluation. Numerous techniques have been used for this purpose. Among the various methods, heat flow determination using thermal gradient/heat flow estimates from deep wells and geothermometer techniques is widely recognized as a reliable approach for geothermal exploration (Alrefaee, 2022). In this method, thermal gradients are measured to create a contour map of heat flow, which provides valuable insights into the distribution of heat in the subsurface of geothermal areas (Ateş et al., 2005).

Gradient data from Korkmaz (2010), Mihçakan et al. (2006) which contain the most comprehensive depth/temperature data capable of reflecting the gradient character of the study area, were used in this paper. Data set 1 is based on temperature gradient data measured in deep wells (between 1000 and 4500 m), while data set 2 is based on shallow wells (between 100 and 150 m). Data set 2 has a relatively more homogeneous distribution than data set 1. However, as the data come from shallow wells, the temperatures obtained are likely to be influenced by groundwater, surface, and climatic effects. The temperatures obtained are certainly more realistic, considering that the data in Data Set 1 were obtained from 1000 m and deeper. A more reliable dataset has been produced by averaging the shallow and deep well data. According to the interpolated data, the gradient varies between 66.28 C $km^{-1}$and 121.68 C $km^{-1}$, with high gradient values seen especially in the western part of the study area (Fig. 8A). The basic statistical analysis and histogram of gradient data calculated in previous studies (Korkmaz, 2010; Mihçakan et al., 2006) are presented in Table A.1 and Fig. A.1, respectively.

Furthermore, the analysis of Curie point depth has been recognized as a valuable technique for estimating the regional thermal structure and heat flow. Studies have shown that the depths inferred by extrapolating geothermal gradient and heat-flow values using Curie point depth analysis provide geologically reasonable results, indicating the utility of this method in estimating heat flow in geothermal areas (Stampolidis et al., 2005). The Dikili-Bergama region, located on the border of the tectonic suture zone, has an approximate Curie point depth value of 6.71 km (Bilim et al., 2016). This shallow value is directly related to the formation of the young graben. The Oligo-Miocene granitoid, which has the largest surface area in western Anatolia, is in the suture zone and has a shallow Curie point depth, allowing for high heat flow values.

The thermal conductivity of volcanic rocks directly affects the heat flow characteristics of the subsurface (Heap et al., 2020; Robertson and Peck, 1974; Кузнецова, 2017), however, the mineralogy, porosity, and alteration of volcanic rocks can all have an impact on the wide range of thermal conductivity values that they display. The thermal conductivity of volcanic rocks with different compositions within the Kıratlı unit in the study area varies between 1.2 $Wm^{-1}K^{-1}$ and 2.2 $Wm^{-1}K^{-1}$. Detailed petrographic studies can be carried out to understand the reasons for this variable result.

Additionally, the role of thermal conductivity in understanding the

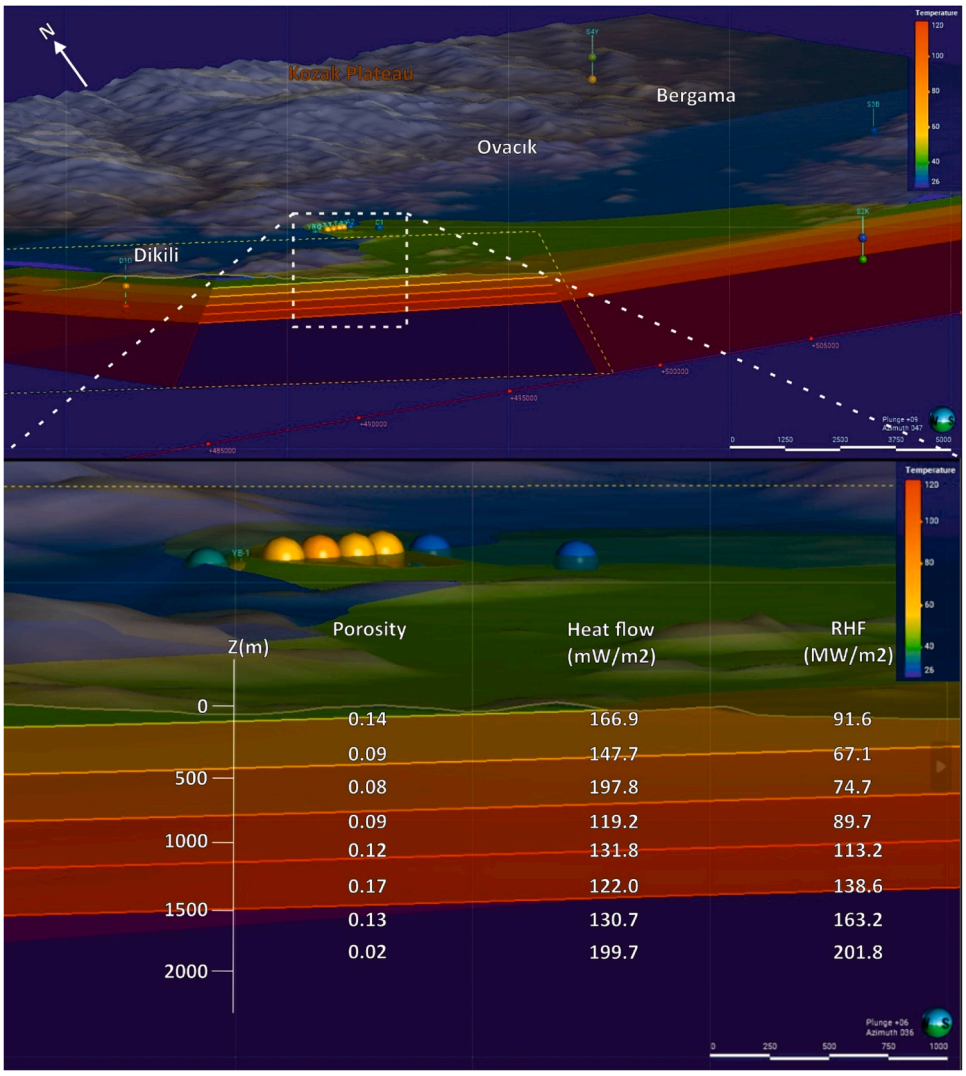


**Fig. 9.** Optimized thermal model (RHF: radioactive heat flow).

advective and conductive heat transport associated with volcanic regions provides insights into the mechanisms of heat transfer and the contribution of radioactive heat flow to the overall thermal regime (Manga, 1998; Okubo and Matsunaga, 1994). Although thermal conductivity varies according to different parameters, radioactive heat production directly relates to lithology. Radioactive heat production (RHP) values of samples collected from different lithologies were calculated with the Rybach (1976) Eq. (5). The RHP of volcanic rocks ranges from 1.1 $\mu Wm^{-3}$ to 7.9 $\mu Wm^{-3}$. The sample from the Kıratlı unit with tephrite composition exhibited the highest RHP. Samples from the Kozak pluton group were measured to have values ranging from 2.7 $\mu Wm^{-3}$ to 7.4 $\mu Wm^{-3}$. The calculated RHP values of metamorphic rocks range from 0.2 $\mu Wm^{-3}$ to 1.2 $\mu Wm^{-3}$. The RHP value increases relatively towards depth when examining the general lithostratigraphic section (Fig. 8B). The surface radioactive heat flow values were calculated using the RHP values measured for each collected sample, following the Lachenbruch (1968) Eq. (6). It is important to note that the calculated radioactive heat flow values are consistent with the heat flow calculated by thermal gradient only in homogeneous lithologies such as granodiorite. Specifically, the calculated RHF values of homogeneous lithologies with low porosity are dependable (Fig. 9).

The relationship between radioactive heat flow and terrestrial heat flow is influenced by several factors, including the chemical composition, mineral content, and thermal conductivity of rocks, as well as the presence of radioactive elements. These factors together contribute to the observed heat flow in the lithosphere. Thermal conductivity, which is crucial for heat flow, is affected by mineral composition, rock structure, porosity, water content, temperature, and pressure conditions. Additionally, the thermal conductivity, specific heat, and thermal diffusivity of rocks are influenced by their chemical composition and mineral content (Li et al., 2023).

This relationship is further emphasized by the fact that surface heat flow is the sum of the heat flow originating from the mantle and the total heat generated by radioactive decay (Sleep, 2009). Variations in thermal conductivity between different stratigraphic sections can result in anomalously high heat flow values, underscoring the role of thermal conductivity in heat flow distribution (Balkan-Pazvantoğlu et al., 2021).

Heat flow values and thermal conductivity are generally positively related, although some samples in the study exhibit varying thermal gradient values. Conversely, these same samples show a negative correlation between radioactive heat flow (RHF) values and thermal conductivity (Fig. 10A–C). Radioactive heat flow results from the decay of radioactive isotopes in rocks, which produce heat. This heat production from radioactive decay does not necessarily align with the thermal conductivity of the rock, leading to the observed negative correlation. Furthermore, the direct relationship between water-saturated thermal conductivity and terrestrial heat flow, calculated using different two-phase models, proved to be a more reliable trend than the inverse

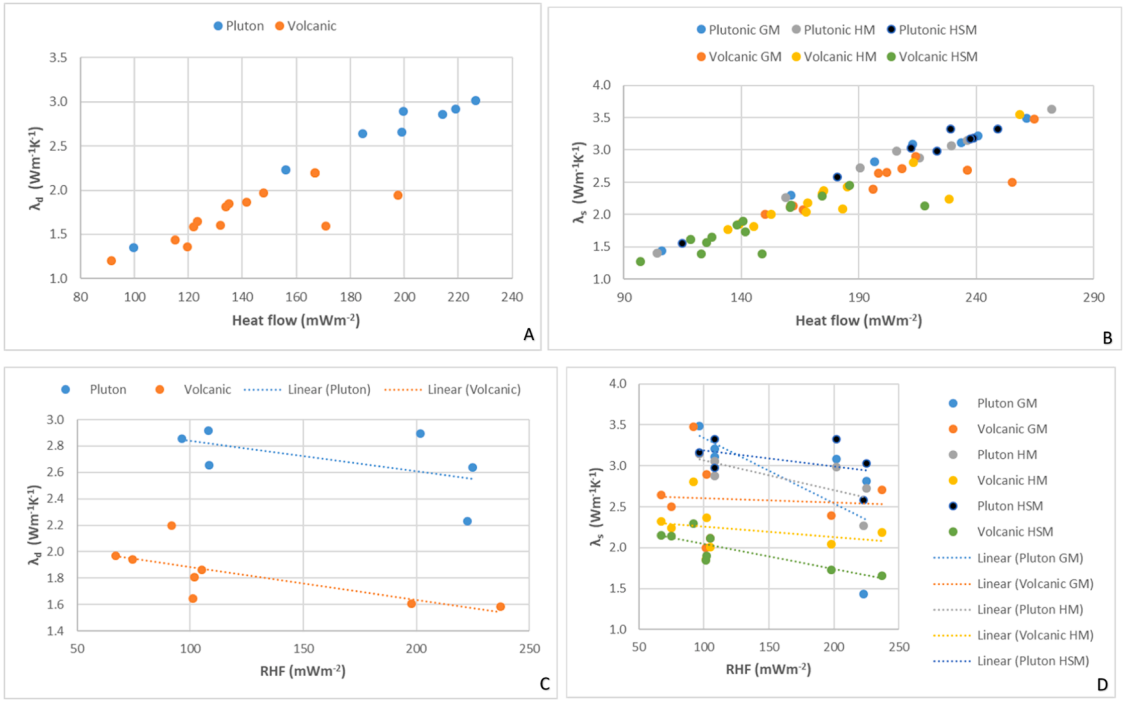


**Fig. 10.** A) Measured thermal conductivity ($\lambda_d$) and heat flow correlation for plutonic and volcanic rocks B) Correlation of calculated water saturation thermal conductivity ($\lambda_s$) and heat flow for plutonic and volcanic rocks C) Measured thermal conductivity ($\lambda_d$) and radioactive heat flow (RHF) correlation for plutonic and volcanic rocks D) Correlation of calculated water saturation thermal conductivity values ($\lambda_s$) and RHF of two-phase system models. GM: Geometric mean HM: Harmonic mean HSM: Hashin and Shtrikman mean.

**Table 3**
Averaged measured thermal conductivity ($\lambda_d$), calculated water saturated thermal conductivity ($\lambda_s$) with two phase models (GM: Geometric mean, HM: Harmonic mean, HSM: Hashin and Strikman mean), porosity, thermal gradient, heat flow (HF) and radioactive heat flow (RHF) for each lithology group in the Dikili-Bergama region.

| Lithology | Pluton | Volcanic | Metamorphic |
|---|---|---|---|
| **$\lambda_d$ (Wm$^{-1}$K$^{-1}$)** | 2.57 | 1.73 | 2.68 |
| **Porosity** | 0.04 | 0.16 | 0.02 |
| **GM $\lambda_s$ (Wm$^{-1}$K$^{-1}$)** | 2.98 | 3.01 | 2.90 |
| **HM $\lambda_s$ (Wm$^{-1}$K$^{-1}$)** | 2.76 | 2.35 | 2.79 |
| **HSM $\lambda_s$ (Wm$^{-1}$K$^{-1}$)** | 2.89 | 1.82 | 3.07 |
| **Thermal gradient (C km$^{-1}$)** | 72.88 | 81.21 | 74.67 |
| **HF$_d$ (mW/m$^2$)** | 187.40 | 140.30 | 200.00 |
| **HF GM (mW/m$^2$)** | 217.43 | 244.55 | 216.27 |
| **HF HM (mW/m$^2$)** | 201.36 | 190.55 | 207.95 |
| **HF HSM (mW/m$^2$)** | 210.84 | 148.11 | 229.03 |
| **RHF (mW/m$^2$)** | 152.40 | 104.00 | 53.60 |

relationship between water-saturated thermal conductivity and radioactive heat flow calculated with those models (Fig. 10B–D).

Heat flow values above the global average align with radioactive heat flow values in non-porous rocks. The lithologies in Soultz-sous-Forêts, where a successful enhanced geothermal systems (EGS) plant is located, exhibit thermal conductivity measurement results similar to those in the Dikili-Bergama region. However, when thermal gradient values are considered, discrepancies arise. The Dikili-Bergama region has an average thermal gradient of 76.3 °C km$^{-1}$ (Table 3), while the Upper Rhine Graben, home to Soultz-sous-Forêts, has an average geothermal gradient of 36.3 °C km$^{-1}$ (Stober and Bucher, 2014). Moreover, the average heat flow for the Soultz-sous-Forêts region is calculated at 155.5 mWm$^{-2}$ (Harlé et al., 2019), compared to 191.6 mWm$^{-2}$ for the Dikili-Bergama region. The active tectonic and volcanic activities present in the region, along with high geothermal gradients and heat flow values, have fostered the development of high-enthalpy geothermal systems, thus contributing to the overall heat flow in western Anatolia.

To determine whether the heat flow originates from radiogenic granites or a heat source related to active tectonism, it is essential to diversify and enrich the data. Geochemical and mineralogical studies are vital for pinpointing the source of heat flow across various geological environments. Investigating relationships between thermal conductivity and petrophysical parameters can enhance our understanding of the thermal properties of reservoir rocks and illustrate the impact of mineralogical composition on heat transfer within geological formations (Zerrouki et al., 2019). In addition, detailed geophysical investigations, such as magnetotelluric analyses, can help ascertain whether the heat source is derived from the Earth's mantle. Predictive models of mineralogy based on whole-rock sample data can also classify alteration assemblages and estimate bulk mineralogy, thereby providing insight into the mineralogical changes associated with heat flow processes (Escolme et al., 2019).

### 5.4. Thermal model

Geothermal studies in the region have highlighted the importance of lithospheric heating by mantle upwelling and magma production, supporting a magma-assisted rifting model in western Anatolia. The crustal velocity model suggests that the lithosphere in the region may have been initially cold and thick, with subsequent heating by mantle upwelling contributing to the observed high heat flows (Akyol et al., 2006). The westward motion of Anatolia and north-south extension, driven by slab rollback processes and episodes of slab tearing, have contributed to the geothermal activity and high heat flow values observed in western Anatolia. High-temperature geothermal systems aligned along the northern and southern edges of detachment faults in western Anatolia are associated with active tectonism (Özdemir et al., 2022). This suggests that the heating source for the high heat flow values in the region is primarily driven by tectonic processes, emphasizing the role of fault structures in facilitating heat transfer. Furthermore, studies of geothermal activity in western Anatolia have highlighted intense

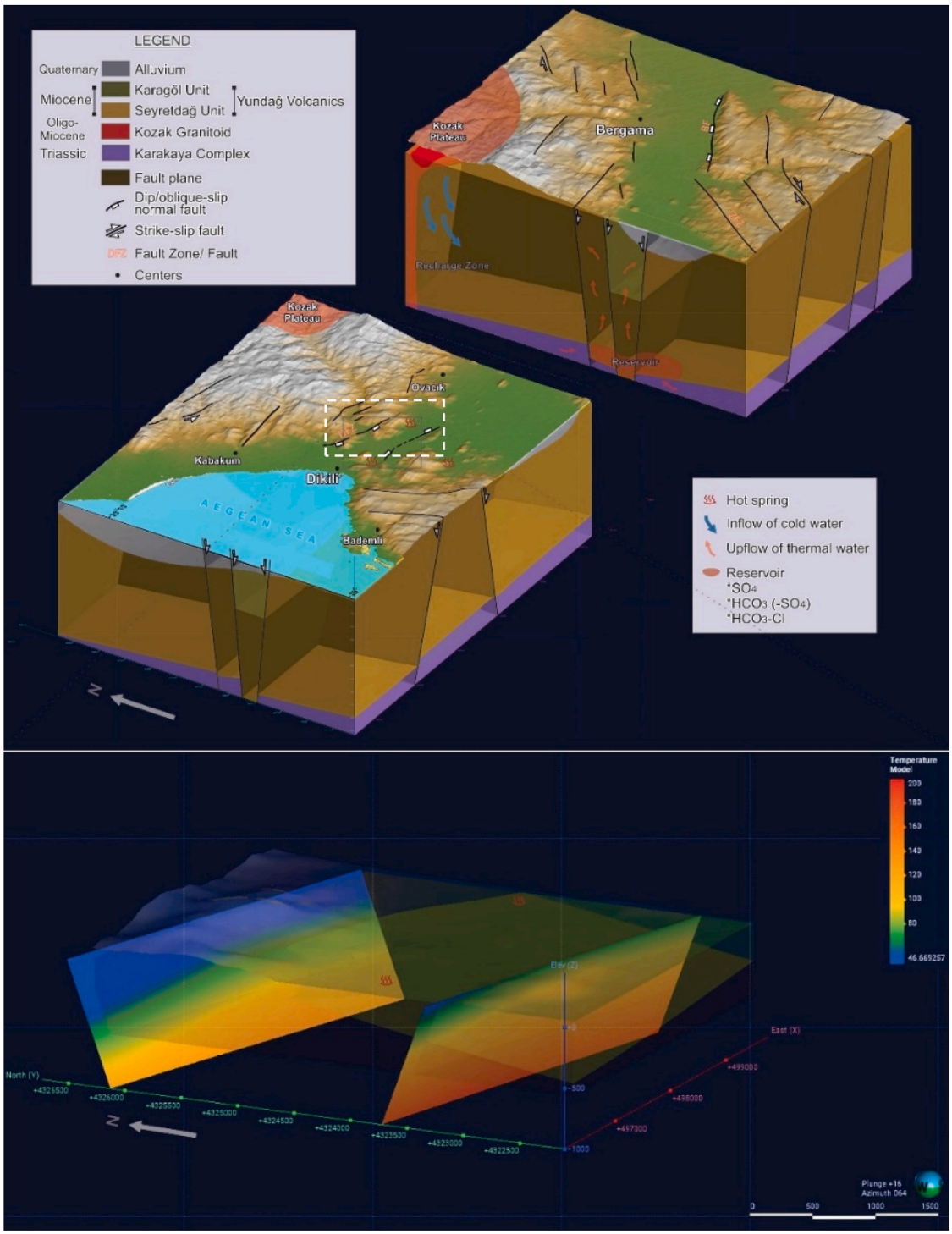


**Fig. 11.** Conceptual geologic model and thermal model of Dikili Fault Zone.

Miocene magmatic activity, which has significantly influenced the region's current tectonic evolution (Roche et al., 2018). Magmatic activity and tectonic extension processes are known to affect heat flow patterns and thermal regimes in regions undergoing lithospheric extension, potentially leading to increased heat flow values.

The Vardar-İzmir-Ankara suture belt, associated with the north-dipping subduction zone, marks the boundary between different tectonic units formed during plate tectonic processes in Neotethys (Schmid et al., 2020). The tectonic evolution associated with the suture zone has likely influenced the structural control of faults, including north-dipping faults, which may contribute to the high heat flows observed in the Dikili-Bergama region. The potential point marked on the conceptual model was determined based on the study data. A thermal modeling was performed at the indicated point. The depth-dependent temperature indicators of the faults in the created model were examined. It is very likely that the north-dipping normal fault, which is part of the Dikili fault zone, achieves a high heat flow at a much shallower depth (Fig. 11). The high heat flow of the north-dipping faults in western Anatolia is mainly due to active tectonism, shear heating due to fault activity caused by the concentration of geothermal systems along the fault structures.

## 6. Conclusions

In this study, 27 rock samples from 2 different lithological groups, namely volcanic and plutonic rocks, from the Dikili-Bergama region, which is located in the West Anatolian extension zone, were analyzed.

The lithological characterization of the rocks was determined during the analysis. Typically, magma from the Earth's mantle interacts with the continental crust and is dominated by calcareous rocks with a high K value, which occurs in regions associated with subduction zones.

The analysis of the thermal conductivity shows that the thermal conductivity decreases with increasing porosity. However, the calculation of the average thermal conductivity of water-saturated samples shows that it is directly proportional to porosity. Moreover, the average thermal conductivity of the water-saturated samples increases with increasing $SiO_2$ value. In addition, the thermal conductivity values for two-phase systems were calculated using the geometric mean, the harmonic mean, and the Hashin and Strikman mean. It should be noted that porosity and $SiO_2$ content are directly related to the GM and HM models, but inversely related to the HSM model. According to the standard deviation value, the HM model proved to be the most reliable model for determining the saturated thermal conductivity of igneous rocks.

A detailed map of the thermal gradient of the study area was created, and values up to 121.68 C $km^{-1}$ were observed in the south western part of the area.

The radioactive heat flow and terrestrial heat flow values reach up to 200 $mWm^{-2}$. The lithological features represented in the thermal model of the region were investigated and it was found that the discrepancy between the radioactive heat flow and the heat flow measurements is directly related to porosity. In order to gain a deeper understanding of the thermal structure of the region, comprehensive thermophysical, structural and petrographic studies need to be carried out.

The Soultz-sous-Forêts geothermal field is a pioneer of EGS technology and generates 12 GWh of electricity annually (Chabab et al., 2021). The potential of the Dikili-Bergama field, which has significantly higher heat flow values, cannot be overlooked to contribute to sustainable geothermal energy production in the future. The thermal model of the potential area depicted on the conceptual model was created using thermal gradient data from deep and shallow wells in the region and provides a data set for future geothermal investigations.

## CRediT authorship contribution statement

**Tolga Ayzit:** Writing – original draft, Visualization, Software, Methodology, Investigation, Data curation, Conceptualization. **Selçuk Erol:** Writing – review & editing, Validation, Methodology. **Alper Baba:** Supervision.

## Declaration of competing interest

The authors declare that they have no known competing financial interests or personal relationships that could have appeared to influence the work reported in this paper.

## Acknowledgments

All analyzes mentioned in the article were obtained thanks to IZTECH Integrated Research Centers (IZTECH IRC). This research did not receive any specific grant from funding agencies in the public, commercial, or not-for-profit sectors. The first author is financially sponsored by the TÜBİTAK Science Fellowships and Grant Program Directorate through 2211 PhD Scholarship Program.

## Supplementary materials

Supplementary material associated with this article can be found, in the online version, at doi:10.1016/j.geothermics.2025.103306.

## Data availability

Data will be made available on request.

## References

Akar, T., Gemici, Ü., Somay-Altaş, M., Tarcan, G., 2021. Numerical Modeling of Fluid Flow and Heat Transfer in Kurşunlu Geothermal Field-KGF (Salihli, Manisa /Turkey). Turkish J. Earth Sci. https://doi.org/10.3906/yer-2106-12.

Akbulut, M., Sümer, Ö., Akal, C., Inaner, H., 2023. Evaluating Geological Heritage Around UNESCO World Heritage Assets: a Study from the Dikili and Madra Mountain (Western Anatolia, İzmir, Türkiye). Geoheritage 15, 59.

Akyol, N., Zhu, L., Mitchell, B.J., Sözbilir, H., Kekovali, K., 2006. Crustal Structure and Local Seismicity in Western Anatolia. Geophys. J. Int. https://doi.org/10.1111/j.1365-246x.2006.03053.x.

Akyürek, B., Soysal, Y., 1980. Main Geological Features of the Area South of Biga Peninsula (Savaştepe-Kırkağaç-Bergama-Ayvalık). Bull. Miner. Res. Explor. 1980, 1.

Aldanmaz, E., 1998. Petrogenesis of late cenozoic collision volcanism in western Anatolia, Turkey. Durham University.

Alrefaee, H.A., 2022. Structural and Stratigraphic Controls on the Geothermal Regime of the Gulf of Suez, Egypt as Revealed by the Geophysical and Bottom-Hole Temperature Data. Egypt. J. Geol. https://doi.org/10.21608/egjg.2023.177487.1031.

Altunkaynak, Ş., Yilmaz, Y., 1998. The mount Kozak magmatic complex, western Anatolia. J. Volcanol. Geotherm. Res. 85, 211–231.

ArcGIS, 2023. Foundational system for GIS & mapping [WWW Document]. URL https://www.esri.com/en-us/arcgis/about-arcgis/overview.

Ateş, A.S., Bilim, F., Büyüksaraç, A., 2005. Curie Point Depth Investigation of Central Anatolia, Turkey. Pure Appl. Geophys. https://doi.org/10.1007/s00024-004-2605-3.

Athens, N.D., Caers, J.K., 2019. A Monte Carlo-based framework for assessing the value of information and development risk in geothermal exploration. Appl. Energy 256, 113932.

Aydın, İ., Karat, H.İ., Koçak, A., 2005. Curie-point depth map of Turkey. Geophys. J. Int. 162, 633–640.

Ayzit, T., Chandrasekharam, D., Baba, A., 2022. Salihli Granitoid, Menderes Massif, Western Anatolia: A sustainable clean energy source for mitigating CO2 emissions. In: International Conference on Natural Resources and Sustainable Environmental Management, pp. 272–283.

Baba, A., Sözbilir, H., Demir, M.M., Akkurt, G.G., Öz\csen, A.Y., \cSener, M.F., Hanc\io \uglu, E., Uzelli, T., 2022. İzmir ilindeki jeotermal kaynakların potansiyeli, kullanım alanları, ekonomik ve çevresel etkilerinin belirlenmesi araştırılması. Proj. Rep. 194.

Balkan-Pazvantoğlu, E., Erkan, K., Şalk, M., Akkoyunlu, B.O., Tayanç, M., 2021. Surface Heat Flow in Western Anatolia (Turkey) and Implications to the Thermal Structure of the Gediz Graben. Turkish J. Earth Sci. https://doi.org/10.3906/yer-2105-28.

Bas, M.J.L.E., Maitre, R.W.Le, Streckeisen, A., Zanettin, B., on the Systematics of Igneous Rocks, I.S., 1986. A chemical classification of volcanic rocks based on the total alkali-silica diagram. J. Petrol. 27, 745–750.

Bilim, F., Akay, T., Aydemir, A., Kosaroglu, S., 2016. Curie point depth, heat-flow and radiogenic heat production deduced from the spectral analysis of the aeromagnetic data for geothermal investigation on the Menderes Massif and the Aegean Region, western Turkey. Geothermics 60, 44–57.

Birkhölzer, J., 2006. A Temperature-Profile Method for Estimating Flow in Geologic Heat Pipes. J. Contam. Hydrol. https://doi.org/10.1016/j.jconhyd.2005.12.009.

Birkholzer, J.T., 2005. Estimating Liquid Fluxes in Thermally Perturbed Fractured Rock Using Measured Temperature Profiles. https://doi.org/10.2172/850438.

Blázquez, C.S., García, P.C., Nieto, I.M., Maté-González, M.Á., Martín, A.F., González-Aguilera, D., 2020. Characterizing Geological Heterogeneities for Geothermal Purposes Through Combined Geophysical Prospecting Methods. Remote Sens. https://doi.org/10.3390/rs12121948.

Borsi, S., Ferrara, G., Innocenti, F., Mazzuoli, R., 1972. Geochronology and petrology of recent volcanics in the Eastern Aegean Sea (West Anatolia and Lesvos Island). Bull. Volcanol. 36, 473–496.

Boztuğ, D., Harlavan, Y., Jonckheere, R., Can, I., Sarı, R., 2008. Geochemistry and K-Ar Cooling Ages of the Ilıca, Çataldağ (Balıkesir) and Kozak (İzmir) Granitoids, West Anatolia, Turkey. Geol. J. https://doi.org/10.1002/gj.1132.

Caineng, Z.O.U., Zhi, Y., Jingwei, C.U.I., Rukai, Z., Lianhua, H., Shizhen, T., Xuanjun, Y., Songtao, W., Senhu, L., Lan, W., 2013. Formation mechanism, geological characteristics and development strategy of nonmarine shale oil in China. Pet. Explor. Dev. 40, 15–27.

Cengiz, M., Karabulut, S., Özçep, F., Çabuk, B.S., Heller, F., 2021. Paleomagnetic Results From Western Anatolia: Evidence of Microblock Rotations After Emplacement of the Lower Miocene Yuntdağ Volcanic Rocks. Ann. Geophys. https://doi.org/10.4401/ag-8699.

Cermak, V., Hurtig, E., 1977. Preliminary heat flow map of Europe. Explanatory text.

Chokphoemphun, S., Pimsarn, M., Thianpong, C., Promvonge, P., 2015. Heat Transfer Augmentation in a Circular Tube With Winglet Vortex Generators. Chinese J. Chem. Eng. https://doi.org/10.1016/j.cjche.2014.04.002.

Chopra, N., Ray, L., Satyanarayanan, M., Elangovan, R., 2018. Evaluate best-mixing model for estimating thermal conductivity for granitoids from mineralogy: a case study for the granitoids of the Bundelkhand craton, central India. Geothermics 75, 1–14.

Daly, R.A., Manger, G.E., Clark, S.P., 1966. Section 4: Density of rocks. Geol. Soc. Am. Mem. 97, 19–26.

Dilek, Y., Altunkaynak, Ş., 2009. Geochemical and Temporal Evolution of Cenozoic Magmatism in Western Turkey: Mantle Response to Collision, Slab Break-Off, and Lithospheric Tearing in an Orogenic Belt. Geol. Soc. London Spec. Publ. https://doi.org/10.1144/sp311.8.
Doğru, F., Pamukçu, O., 2019. Analysis of Gravity Disturbance for Boundary Structures in the Aegean Sea and Western Anatolia. Geofizika. https://doi.org/10.15233/gfz.2019.36.5.
Dolmaz, M.N., Hisarlı, Z.M., Ustaömer, T., Orbay, N., 2005. Curie Point Depths Based on Spectrum Analysis of Aeromagnetic Data, West Anatolian Extensional Province, Turkey. Pure Appl. Geophys. https://doi.org/10.1007/s00024-004-2622-2.
Eken, T., 2019. Moment Magnitude Estimates for Central Anatolian Earthquakes Using Coda Waves. Solid Earth. https://doi.org/10.5194/se-10-713-2019.
Ercan, T., Türkö\ugen, A., Akyürek, B., Günay, E., Çam, A., Ate\cs, M., Can, B., Erkan, M., Özkiri\csçi, C., 1984. Dikili-Bergama-Çandarlı (Batı Anadolu) Yöresinin Jeolojisi ve Magmatik Kayaçlarının Petrolojisi. Jeol. Mühendisliği Derg. 8, 47–60.
Erentöz, C., Ternek, Z., 1968. Türkiye'de termomineral kaynaklar ve jeotermik enerji etüdleri. Bull. Miner. Res. Explor. 70, 1–57.
Erkan, K., 2015. Geothermal Investigations in Western Anatolia Using Equilibrium Temperatures From Shallow Boreholes. Solid Earth. https://doi.org/10.5194/se-6-103-2015.
Erman, C., Yolsal-Çevikbilen, S., Eken, T., Tilmann, F., Keleş, D., Taymaz, T., 2022. Constraints on the Lithospheric Kinematics in the Aegean and Western Anatolia Unveiled by SKS Splitting Observations. J. Geophys. Res. Solid Earth. https://doi.org/10.1029/2022jb025265.
Escolme, A., Berry, R.F., Hunt, J.S., Halley, S., Potma, W., 2019. Predictive Models of Mineralogy From Whole-Rock Assay Data: Case Study From the Productora Cu-Au-Mo Deposit, Chile. Econ. Geol. https://doi.org/10.5382/econgeo.2019.4650.
Feng, Z.-Z., Bai, Z., Zhong, H., Zhu, W., Zheng, S.-J., 2020. Genesis of Volcanic Rocks in the Zijinshan Ore District, SE China: Implications for Porphyry-Epithermal Mineralization. Minerals. https://doi.org/10.3390/min10020200.
Fuchs, S., Förster, H.J., Braune, K., Förster, A., 2018. Calculation of Thermal Conductivity of Low-Porous, Isotropic Plutonic Rocks of the Crust at Ambient Conditions From Modal Mineralogy and Porosity: A Viable Alternative for Direct Measurement? J. Geophys. Res. Solid Earth 123, 8602–8614. https://doi.org/10.1029/2018JB016287.
Fuchs, S., Norden, B., Neumann, F., Kaul, N., Tanaka, A., Kukkonen, I.T., Pascal, C., Christiansen, R., Gola, G., Šafanda, J., 2023. Quality-assurance of heat-flow data: The new structure and evaluation scheme of the IHFC Global Heat Flow Database. Tectonophysics 863, 229976.
Fuchs, S., Schütz, F., Förster, H.-J., Förster, A., 2013. Evaluation of common mixing models for calculating bulk thermal conductivity of sedimentary rocks: correction charts and new conversion equations. Geothermics 47, 40–52.
Görür, N., Şengör, A.M.C., Sakinü, M., Akkök, R., Yiğitbaş, E., Oktay, F.Y., Barka, A., Sarica, N., Ecevitoğlu, B., Demirbağ, E., Ersoy, Ş., Algan, O., Güneysu, C., Aykol, A., 1995. Rift Formation in the Gökova Region, Southwest Anatolia: Implications for the Opening of the Aegean Sea. Geol. Mag. https://doi.org/10.1017/s0016756800018884.
Graessner, T., Schenk, V., Bröcker, M., Mezger, K., 2000. Geochronological Constraints on the Timing of Granitoid Magmatism, Metamorphism and Post-metamorphic Cooling in the Hercynian Crustal Cross-section of Calabria. J. Metamorph. Geol. https://doi.org/10.1046/j.1525-1314.2000.00267.x.
Gröber, H., Erk, S., 2013. Die grundgesetze der wärmeübertragung. Springer-Verlag.
Gürer, D., Hinsbergen, D.J.J.van, Özkaptan, M., Creton, I., Koymans, M., Cascella, A., Langereis, C.G., 2018. Paleomagnetic Constraints on the Timing and Distribution of Cenozoic Rotations in Central and Eastern Anatolia. Solid Earth. https://doi.org/10.5194/se-9-295-2018.
Harlé, P., Kushnir, A.R.L., Aichholzer, C., Heap, M.J., Hehn, R., Maurer, V., Baud, P., Richard, A., Genter, A., Duringer, P., 2019. Heat flow density estimates in the Upper Rhine Graben using laboratory measurements of thermal conductivity on sedimentary rocks. Geotherm. Energy 7, 1–36.
Heap, M., Kushnir, A., Vasseur, J., Wadsworth, F.B., Harlé, P., Baud, P., Kennedy, B., Troll, V.R., Deegan, F.M., 2020. The Thermal Properties of Porous Andesite. J. Volcanol. Geotherm. Res. https://doi.org/10.1016/j.jvolgeores.2020.106901.
Hogarth, R.A., Bour, D., 2015. Flow performance of the Habanero EGS closed loop. In: Proceedings of World Geothermal Congress.
Hou, Z., Şen, O., Gou, Y., Eker, A.M., Li, M., Yal, G.P., Cambazoğlu, S., Were, P., 2015. Preliminary Geological, Geochemical and Numerical Study on the First EGS Project in Turkey. Environ. Earth Sci. https://doi.org/10.1007/s12665-015-4407-6.
Huang, Y., Ye, C., Ren, L., Tian, F., Pan, S., Wang, K., Wang, J., Dong, Y., Kong, Y., 2022. Assessing the Geothermal Resource Potential of an Active Oil Field by Integrating a 3D Geological Model With the Hydro-Thermal Coupled Simulation. Front. Earth Sci. https://doi.org/10.3389/feart.2021.787057.
Ilkışık, O.M., 1992. Silica heat flow estimates and lithospheric temperature in Anatolia. In: Proceedings, XI. Congress of World Hydrothermal Organization. Istanbul, May, pp. 92–104.
Jatmiko, B.W., Assiddiqy, M.H., Ediatmaja, P., Prabowo, R., Sutopo, S., Pratama, H.B., Hamdani, M.R., 2022. Resource Assessment of Ungaran Geothermal Field Using Numerical Model and Monte Carlo Simulation. Iop Conf. Ser. Earth Environ. Sci. https://doi.org/10.1088/1755-1315/1031/1/012021.
Johnson, G.R., Olhoeft, G.R., 2017. Density of rocks and minerals. Handbook of Physical Properties of Rocks (1984). CRC Press, pp. 1–38.
Karacik, Z., Yilmaz, Y., Pearce, J.A., 2007. The Dikili-Çandarlı volcanics, Western Turkey: magmatic interactions as recorded by petrographic and geochemical features. Turkish J. Earth Sci. 16, 493–522.
Karat, H.I., Aydın, I., 2004. Report on preparation of the curie isotherm depth Map of Turkey. Unpubl. Rep.
Komut, T., Gray, R., Pysklywec, R.N., Gogus, O., 2012. Mantle Flow Uplift of Western Anatolia and the Aegean: Interpretations From Geophysical Analyses and Geodynamic Modeling. J. Geophys. Res. Atmos. https://doi.org/10.1029/2012jb009306.
Kong, Y., Pan, S., Ren, Y., Zhang, W., Wang, K., Jiang, G., Cheng, Y., Sun, W., Zhang, C., Hu, S., 2021. Catalog of Enhanced Geothermal Systems based on Heat Sources. Acta Geol. Sin. Ed. 95, 1882–1891.
Korkmaz, D., 2010. Türkiye Jeotermal Enerji Potansiyelinin Araastirilmasi. Doktora Tezi, İstanbul Teknik Üniversitesi Fen Bilimleri Enstitüsü.
Kothari, R., Hemmingsen, C.S., Voigt, N.V., La Seta, A., Nielsen, K.K., Desai, N.B., Vijayan, A., Haglind, F., 2024. Numerical and experimental analysis of instability in high temperature packed-bed rock thermal energy storage systems. Appl. Energy 358, 122535.
Kurek, K.A., 2021. Geothermal resources and local development in Poland 214.
Кузнецова, E.M., 2017. Thermal Conductivity and the Unfrozen Water Contents of Volcanic Ash Deposits in Cold Climate Conditions: A Review. Clays Clay Miner. https://doi.org/10.1346/ccmn.2017.064057.
Kyoto, 2020. Thermal measuring instruments [WWW Document]. URL https://www.kem.kyoto/en/.
Lachenbruch, A.H., 1968. Preliminary geothermal model of the Sierra Nevada. J. Geophys. Res. 73, 6977–6989. https://doi.org/10.1029/JB073I022P06977.
Lemmon, E.W., 2010. Thermophysical properties of fluid systems. NIST Chem. Webb.
Li, K., Zhang, Y., He, Q., Zhang, S., Jia, W., He, X., Zhang, H., Wang, L., Wang, S., 2023. Characteristics of Thermophysical Parameters in the Wugongshan Area of South China and Their Insights for Geothermal Genesis. Front. Environ. Sci. https://doi.org/10.3389/fenvs.2023.1112143.
Liu, Y., Guo, L., Wang, Y., Liao, Y., Zhao, G.F., 2022. Numerical Simulation and Design Optimization of Large-Scale Geothermal Production Based on a Multiwell Layout in Xianxian Geothermal Field. Lithosphere. https://doi.org/10.2113/2022/2929551.
Liu, Y., Liu, G., Zhao, Z., Hong-liang, Z., 2019. Theoretical Model of Geothermal Tail Water Reinjection Based on an Equivalent Flow Channel Model: A Case Study in Xianxian, North China Plain. Energy Explor. & Exploit. https://doi.org/10.1177/0144598718822401.
Lucazeau, F., 2019. Analysis and Mapping of an Updated Terrestrial Heat Flow Data Set. Geochemistry Geophys. Geosystems. https://doi.org/10.1029/2019gc008389.
Lund, J.W., Toth, A.N., 2021. Direct utilization of geothermal energy 2020 worldwide review. Geothermics 90. https://doi.org/10.1016/j.geothermics.2020.101915.
Lyu, C., Wang, X., Lu, X., Zhou, Q., Zhang, Y., Sun, Z., Xiao, L., Liu, X., 2020. Evaluation of Hydrocarbon Generation Using Structural and Thermal Modeling in the Thrust Belt of Kuqa Foreland Basin, NW China. Geofluids. https://doi.org/10.1155/2020/8894030.
Manga, M., 1998. Advective Heat Transport by Low-Temperature Discharge in the Oregon Cascades. Geology. https://doi.org/10.1130/0091-7613.
Martuganova, E., Krawczyk, C.M., 2021. 3D Deep Geothermal Reservoir Imaging With Wireline Distributed Acoustic Sensing in Two Boreholes. https://doi.org/10.5194/se-2021-138.
Meixner, T., Gibson, H., Seikel, R., Fitzgerald, D., Stuewe, K., Lane, R., 2010. Stochastic Temperature, Heat Flow and Geothermal Gradient Modeling Direct From a 3D Map of the Cooper Basin Region. Central Australia. https://doi.org/10.1190/1.3513037.
Mihçakan, M., Onur, M., Erçelebi, S.G., Okay, A., Yilmazer, M., 2006. Türkiye Yer altı Sıcaklık Gradyanı Dağılımının Derin Kuyu Sıcaklıkları ve Variogram Analizi Kullanılarak Haritalanması. Tübitak Projesi No YDABÇAG-100Y040, Kasım.
Mutlu, A.K., Karabulut, H., 2011. Anisotropic Pn Tomography of Turkey and Adjacent Regions. Geophys. J. Int. https://doi.org/10.1111/j.1365-246x.2011.05235.x.
Okay, A.I., 2000. Was the Late Triassic orogeny in Turkey caused by the collision of an oceanic plateau? Geol. Soc. London, Spec. Publ. 173, 25–41.
Okay, A.I., Tüysüz, O., 1999. Tethyan sutures of northern Turkey. Geol. Soc. London, Spec. Publ. 156, 475–515.
Okubo, Y., Matsunaga, T., 1994. Curie Point Depth in Northeast Japan and Its Correlation With Regional Thermal Structure and Seismicity. J. Geophys. Res. Atmos. https://doi.org/10.1029/94jb01336.
Özdamar, Ş., Zou, H., Billor, M.Z., Hames, W., Roden, M.F., Sarıkaya, O., Georgiev, S., 2023. Petrogenesis, geochronology and thermochronology of Oligocene to Miocene Western Anatolia granitoid plutons in Turkey. Lithos 107430.
Özdemir, A., Palabiyik, Y., ARABACI, F., 2022. Structural Controls of High-Temperature and Deep Geothermal Systems Associated With Detachment Fault. Eur. J. Tech. https://doi.org/10.36222/ejt.955186.
Özürlan, G., Candansayar, M.E., Şahin, M., 2006. Deep Resistivity Structure of the Dikili-Bergama Region, West Anatolia, Revealed by Two- Dimensional Inversion of Vertical Electrical Sounding Data. Geophys. Prospect. https://doi.org/10.1111/j.1365-2478.2006.00525.x.
Pandarinath, K., 2010. Solute Geothermometry of Springs and Wells of the Los Azufres and Las Tres Vírgenes Geothermal Fields. Mexico. Int. Geol. Rev. https://doi.org/10.1080/00206810903442014.
Pourhakkak, P., Taghizadeh, A., Taghizadeh, M., Ghaedi, M., Haghdoust, S., 2021. Fundamentals of adsorption technology. Interface Sci. Technol. 33, 1–70. https://doi.org/10.1016/B978-0-12-818805-7.00001-1.
Prol-Ledesma, R.M., Arango-Galván, C., Torres-Vera, M.A., 2016. Rigorous Analysis of Available Data From Cerro Prieto and Las Tres Virgenes Geothermal Fields With Calculations for Expanded Electricity Generation. Nat. Resour. Res. https://doi.org/10.1007/s11053-016-9295-2.
Putra, H.N.A., Wahyudi, W., 2021. The Estimation of Subsurface Structure Within Geothermal Manifestation Area as an Outflow Zone Using Geoelectrical Resistivity Method in Tegal, Jawa Tengah. Geoeco. https://doi.org/10.20961/ge.v7i1.42392.

Qiao, Y., Zuo, Y., Tu, S., Zhang, J., Yang, M., Zhang, T., 2023. Strata Temperatures and Geothermal Resource Evaluation in the Dongpu Depression, Bohai Bay Basin, North China. Sci. Rep. https://doi.org/10.1038/s41598-023-30760-3.

Ray, L., Förster, H.-J., Förster, A., Fuchs, S., Naumann, R., Appelt, O., 2015. Tracking the thermal properties of the lower continental crust: Measured versus calculated thermal conductivity of high-grade metamorphic rocks (Southern Granulite Province, India). Geothermics 55, 138–149.

Robertson, E.C., Peck, D.L., 1974. Thermal Conductivity of Vesicular Basalt From Hawaii. J. Geophys. Res. Atmos. https://doi.org/10.1029/jb079i032p04875.

Roche, V., Bouchot, V., Beccaletto, L., Jolivet, L., Guillou-Frottier, L., Tuduri, J., Bozkurt, E., Oguz, K., Tokay, B., 2018. Structural, Lithological, and Geodynamic Controls on Geothermal Activity in the Menderes Geothermal Province (Western Anatolia, Turkey). Int. J. Earth Sci. https://doi.org/10.1007/s00531-018-1655-1.

Rybach, L., 1976. Radioactive heat production in rocks and its relation to other petrophysical parameters. Pure Appl. Geophys. 114, 309–317.

Saibi, H., Ehara, S., 2010. Temperature and Chemical Changes in the Fluids of the Obama Geothermal Field (SW Japan) in Response to Field Utilization. Geothermics. https://doi.org/10.1016/j.geothermics.2010.06.005.

Schmid, S.M., Fügenschuh, B., Kounov, A., Maţenco, L., Nievergelt, P., Oberhänsli, R., Pleuger, J., Schefer, S., Schuster, R., Tomljenović, B., Ustaszewski, K., Hinsbergen, D. J.J.van, 2020. Tectonic Units of the Alpine Collision Zone Between Eastern Alps and Western Turkey. Gondwana Res. https://doi.org/10.1016/j.gr.2019.07.005.

Seequent, 2023. Leapfrog Energy 2023.2.1 [WWW Document]. URL https://my.seequent.com/products.

Sleep, N.H., 2009. Stagnant Lid Convection and the Thermal Subsidence of Sedimentary Basins With Reference to Michigan. Geochemistry Geophys. Geosystems. https://doi.org/10.1029/2009gc002881.

Stampolidis, A., Kane, I.A., Τσοκας, Γ.Ν., Τσούρλος, Π., 2005. Curie Point Depths of Albania Inferred From Ground Total Field Magnetic Data. Surv. Geophys. https://doi.org/10.1007/s10712-005-7886-2.

Stober, I., Bucher, K., 2014. Hydraulic and Hydrochemical Properties of Deep Sedimentary Reservoirs of the Upper Rhine Graben. Europe. Geofluids. https://doi.org/10.1111/gfl.12122.

Stolper, E.M., Baker, M.B., Newcombe, M., Schmidt, M.E., Treiman, A.H., Cousin, A., Dyar, M.D., Fisk, M., Gellert, R., King, P.L., Leshin, L.A., Maurice, S., McLennan, S. M., Minitti, M.E., Perrett, G.M., Rowland, S.K., Sautter, V., Wiens, R.C., Bridges, N. T., Johnson, J.R., Cremers, D.A., Bell, J.F., Edgar, L.A., Farmer, J.D., Godber, A., Wadhwa, M., Wellington, D., McEwan, I., Newman, C.E., Richardson, M.E., Charpentier, A., Péret, L., Blank, J., Weigle, G., Li, S., Milliken, R.E., Robertson, K., Sun, V.Z., Edwards, C.S., Farley, K.A., Griffes, J.L., Grotzinger, J.P., Miller, H., Pilorget, C., Rice, M.S., Siebach, K.L., Stack, K., Brunet, C., Hipkin, V., Léveillé, R., Marchand, G., Sánchez, P.S., Favot, L., Cody, G.D., Steele, A., Flückiger, L., Lees, D., Nefian, A., Martin, M., Gailhanou, M., Westall, F., Agard, C., Baroukh, J., Donny, C., Gaboriaud, A., Guillemot, P., Lafaille, V., Lorigny, E., Paillet, A., Perez, R., Saccoccio, M., Yana, C., Armiens-Aparicio, C., Rodríguez, J.C., Blázquez, I.C., Gómez, F., Gómez-Elvira, J., Hettrich, S., Malvitte, A.L., Jiménez, M.M., Martínez-Frías, J., Martín-Soler, J., Martín-Torres, F.J., Jurado, A.M., Mora-Sotomayor, L., Muñoz, G. M., López, S.N., Peinado-González, V., Pla-García, J., Manfredi, J.A.R., Romeral-Planelló, J.J., Fuentes, S.A.S., Martínez, E.S., Redondo, J.T., Urqui-O'Callaghan, R., Mier, M.-P.Z., Chipera, S.J., Lacour, J.-L., Mauchien, P., Sirven, J.-B., Manning, H., Fairén, A.G., Hayes, A.G., Joseph, J., Squyres, S.W., Sullivan, R., Thomas, P.C., Dupont, A., Lundberg, A., Melikechi, N., Mezzacappa, A., DeMarines, J., Grinspoon, D., Reitz, G., Prats, B., Genzer, M., Harri, A., Haukka, H., Kahanpää, H., Kauhanen, J., Kemppinen, O., Paton, M., Polkko, J., Schmidt, W., Siili, T., Fabre, C., Wray, J.J., Poitrasson, F., Patel, K., Gorevan, S., Indyk, S., Paulsen, G., Gupta, S., Bish, D.L., Schieber, J., Gondet, B., Langevin, Y., Geffroy, C., Baratoux, D., Berger, G., Cros, A., d'Uston, C., Forni, O., Gasnault, O., Lasue, J., Lee, Q.-M., Meslin, P., Pallier, E., Parot, Y., Pinet, P., Schröder, S., Toplis, M.J., Lewin, É., Brunner, W., Heydari, E., Achilles, C.N., Oehler, D.Z., Sutter, B., Cabane, M., Coscia, D., Israël, G., Szopa, C., Teinturier, S., Dromart, G., Robert, F., Mouëlic, S. Le, Mangold, N., Nachon, M., Buch, A., Stalport, F., Coll, P., François, P., Raulin, F., Cameron, J.F., Clegg, S., Delapp, D., Dingler, R., Jackson, R., Johnstone, S., Lanza, N., Little, C., Nelson, T., Williams, R., Kirkland, L.E., Baker, B., Cantor, B.A., Caplinger, M., Davis, S.D., Duston, B., Edgett, K.S., Fay, D., Hardgrove, C., Harker, D., Herrera, P., Jensen, E., Kennedy, M.R., Krezoski, G., Krysak, D., Lipkaman, L., Malin, M.C., McCartney, E., McNair, S., Nixon, B., Posiolova, L., Ravine, M.A., Salamon, A., Saper, L., Stoiber, K., Supulver, K., Beek, J. Van, Beek, T. Van, Zimdar, R., French, K.L., Iagnemma, K., Miller, K., Summons, R.E., Goesmann, F., Goetz, W., Hviid, S.F., Johnson, M., Lefavor, M., Lyness, E., Breves, E.A., Fassett, C.I., Blake, D.F., Bristow, T.F., DesMarais, D.J., Edwards, L., Haberle, R.M., Hoehler, T.M., Hollingsworth, J., Kahre, M.A., Keely, L., McKay, C.P., Wilhelm, M.B., Bleacher, L. V, Brinckerhoff, W.B., Choi, D., Conrad, P.G., Dworkin, J.P., Eigenbrode, J., Floyd, M., Freissinet, C., Garvin, J.B., Glavin, D.P., Harpold, D., Mahaffy, P., Martin, D.K., McAdam, A.C., Pavlov, A.A., Raaen, E., Smith, M.D., Stern, J.C., Tan, F., Trainer, M.G., Meÿer, M.A., Posner, A., Voytek, M.A., Anderson, R.C., Aubrey, A.D., Beegle, L.W., Behar, A., Blaney, D.L., Brinza, D.E., Calef, F., Christensen, L.E., Crisp, J.A., DeFlores, L., Ehlmann, B.L., Feldman, J., Feldman, S., Flesch, G.J., Hurowitz, J.A., Jun, I., Keymeulen, D., Maki, J.N., Mischna, M.A., Morookian, J.M., Parker, T.J., Pavri, B., Schoppers, M., Sengstacken, A., Simmonds, J.J., Spanovich, N., Juárez, M. de la T., Vasavada, A.R., Webster, C.R., Yen, A.S., Archer, P.D., Cucinotta, F.A., Jones, J.H., Ming, D.W., Morris, R. V, Niles, P.B., Rampe, E.B., Nolan, T., Radziemski, L.J., Barraclough, B.L., Bender, S., Berman, D.C., Dobrea, E.N., Tokar, R.L., Vaniman, D.T., Williams, R.M.E., Yingst, A., Lewis, K.W., Cleghorn, T., Huntress, W.T., Manhès, G., Hudgins, J., Olson, T.S., Stewart, N., Sarrazin, P., Grant, J.A., Vicenzi, E.P., Wilson, S.A., Bullock, M.A., Ehresmann, B., Hamilton, V.E., Hassler, D.M., Peterson, J., Rafkin, S., Zeitlin, C., Fedosov, F., Golovin, D. V, Karpushkina, N., Kozyrev, A., Litvak, M.L., Malakhov, A., Митрофанов, И.Г., Мокроусов, М.И., Nikiforov, S., Прохоров, В.А., Санин, А.Б., Tretyakov, V.I., Varenikov, A., Vostrukhin, A., Clark, B.C., Wolff, M., Botta, O., Drake, D.M., Bean, K., Lemmon, M.T., Schwenzer, S.P., Anderson, R.B., Herkenhoff, K.E., Lee, E.M., Sucharski, R., Hernández, M.Á. de P., Ávalos, J.J.B., Ramos, M., Jones, A., Kim, M., Malespin, C.A., Plante, I., Müller, J.-P., Navarro-González, R., Ewing, R.C., Boynton, W. V, Downs, R.T., Fitzgibbon, M., Harshman, K., Morrison, S. M., Dietrich, W.E., Kortmann, O., Palucis, M.C., Sumner, D.Y., Williams, A.J., Lugmair, G.W., Wilson, M., Rubin, D.M., Jakosky, B.M., Balić-Žunić, T., Frydenvang, J., Jensen, J.K., Kinch, K.M., Koefoed, A., Madsen, M.B., Stipp, S.L.S., Boyd, N., Campbell, J.L., Pradler, I., VanBommel, S.J., Jacob, S., Owen, T., Atlaskin, E., Savijärvi, H., Boehm, E., Böttcher, S., Burmeister, S., Guo, J., Köhler, J., García, C.M., Mueller-Mellin, R., Wimmer-Schweingruber, R.F., Bridges, J.C., McConnochie, T.H., Benna, M., Franz, H.B., Bower, H., Brunner, A., Blau, H., Boucher, T., Carmosino, M., Atreya, S.K., Elliott, H., Halleaux, D., Rennó, N.O., Wong, M.H., Pepin, R.O., Elliott, B., Spray, J.G., Thompson, L.M., Gordon, S., Newsom, H.E., Ollila, A., Williams, J., Vasconcelos, P.M., Bentz, J., Nealson, K.H., Popa, R., Kah, L.C., Moersch, J., Tate, C. G., Day, M., Kocurek, G., Hallet, B., Sletten, R.S., Francis, R., McCullough, E., Cloutis, E.A., Kate, I.L. ten, Kuzmin, R.O., Arvidson, R.E., Fraeman, A.A., Scholes, D., Slavney, S., Stein, T., Ward, J., Berger, J.A., Moores, J.E., 2013. The Petrochemistry of Jake_M: A Martian Mugearite. Science (80-. ). https://doi.org/10.1126/science.1239463.

Streckeisen, A.L., 1967. Classification and nomenclature of igneous rockes. N. Jb. Miner. 107, 144–240.

Suzuki, Y., Muraoka, H., Asanuma, H., 2020. Validation and Evaluation of an Estimation Method for Deep Thermal Structures Using an Activity Index in Major Geothermal Fields in Northeastern Japan. Energies. https://doi.org/10.3390/en13184684.

Tezcan, A.K., 1979. Geothermal studies, their present status and contribution to heat flow contouring in Turkey. Terrestrial Heat Flow in Europe. Springer, pp. 283–292.

Tezel, T., Shibutani, T., Kaypak, B., 2013. Crustal thickness of Turkey determined by receiver function. J. Asian Earth Sci. 75, 36–45. https://doi.org/10.1016/j.jseaes.2013.06.016.

Turan, A., Artun, E., Saner, S., 2021. Probabilistic Assessment of Geothermal Resources and Their Development in Dikili-İzmir Region. Sn Appl. Sci. https://doi.org/10.1007/s42452-021-04603-7.

Unalan, G., Ongur, T., 1982. Geothermal gradient and temperature investigation at 1000 M depth at some of basin of Turkey. In: GEOGOME-I. Geological Congress of the Middle East. 1, pp. 637–650.

Wang, S., Liu, Z., Shao, J., 2017. Hydrochemistry and H-O-C-S Isotopic Geochemistry Characteristics of Geothermal Water in Nyemo-Nagqu. Tibet. Acta Geol. Sin. - English Ed. https://doi.org/10.1111/1755-6724.13123.

Xing, H., Liu, Y., Gao, J., Chen, S., 2015. Recent Development in Numerical Simulation of Enhanced Geothermal Reservoirs. J. Earth Sci. https://doi.org/10.1007/s12583-015-0506-2.

Yu, J., Zhang, J., Bao-Ping, S., 2010. A Study on Tectono-Thermal Evolution History of Bachu Uplift in the Tarim Basin. Chinese J. Geophys. https://doi.org/10.1002/cjg2.1550.

Zerrouki, A.A., Géraud, Y., Diraison, M., Baddari, K., 2019. A Preliminary Study of Relationships Between Thermal Conductivity and Petrophysical Parameters in Hamra Quartzites Reservoir, Hassi Messaoud Field (Algeria). J. African Earth Sci. https://doi.org/10.1016/j.jafrearsci.2019.01.005.

Zhu, Z., Liu, X., Xu, N., Shao, D., Jiang, X.J., Wu, X., 2020. Integration of 3D Geological Modeling and Geothermal Field Analysis for the Evaluation of Geothermal Reserves in the Northwest of Beijing Plain, China. Water. https://doi.org/10.3390/w12030638.

Zuo, Y., Jiang, S., Shi-hu, W.U., Xu, W., Zhang, J., Feng, R., Yang, M., Zhou, Y., Santosh, M., 2020. Terrestrial Heat Flow and Lithospheric Thermal Structure in the Chagan Depression of the Yingen-Ejinaqi Basin, North Central China. Basin Res. https://doi.org/10.1111/bre.12430.